

Lecture notes Santiago de Chile

Electromagnetic Methods in Geophysics

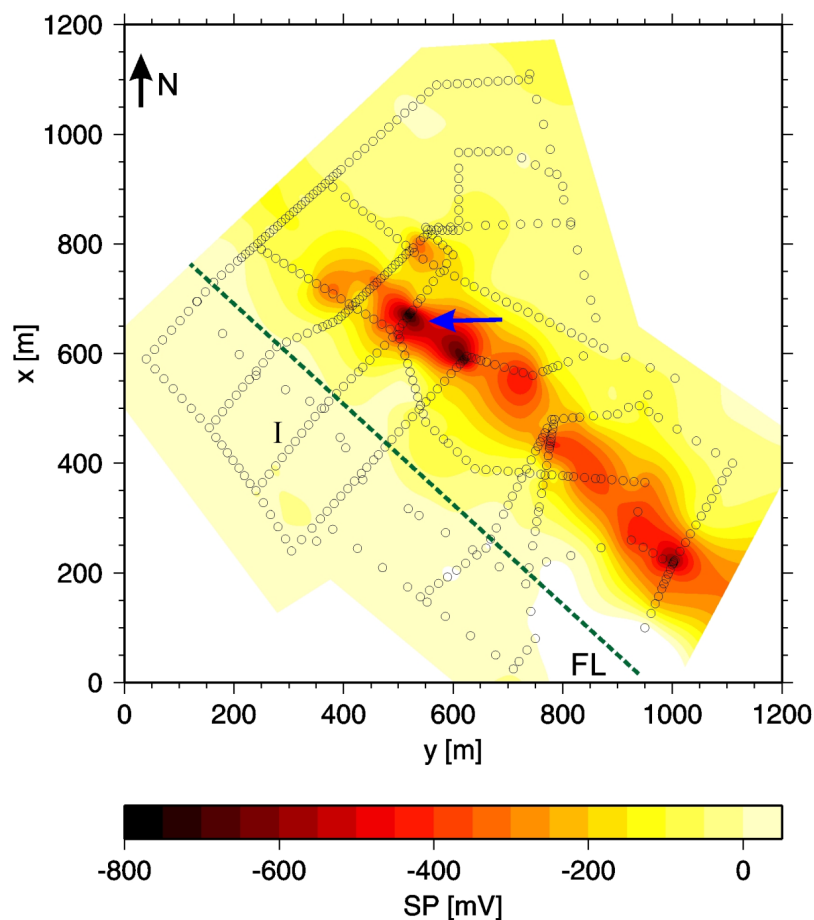
Part II: Overview of other Methods

October 2011

Heinrich Brasse
Fachrichtung Geophysik
Freie Universität Berlin
Malteserstr. 74-100
D-12249 Berlin
Germany

Email: heinrich.brasse@fu-berlin.de

Web: <http://userpage.fu-berlin.de/~hbrasse>



A self-potential anomaly at the Franconian Line in Bavaria

8 DC geoelectric sounding

DC geoelectrics is one of the oldest geophysical exploration techniques, going back to the early decades of last century. It consists basically of feeding a (direct) current into the ground and measuring the resulting voltage drop. Common abbreviations found in literature are VES (vertical electrical sounding) or DCR (direct current resistivity method).

First we'll derive the electric potential in homogeneous and isotropic media. With scalar conductivity $\sigma = \text{const.}$

$$\underline{J} = \sigma \underline{E}$$

A stationary electric field is conservative:

$$\oint_K \underline{E} \cdot d\underline{s} = 0$$

i.e., work is path-independent. With Stokes' theorem:

$$\oint_K \underline{E} \cdot d\underline{s} = \int_A \text{rot} \underline{E} \cdot d\underline{A}$$

(the curve K encompasses area A) it follows:

$$\text{rot} \underline{E} = \nabla \times \underline{E} = 0 \quad ,$$

\underline{E} is thus rotation-free. A rotation-free field may always be represented by a gradient of a scalar potential:

$$\text{rot grad } U = \nabla \times \nabla U = 0$$

$$\Rightarrow \underline{E} = \underline{E}(\underline{r}) = -\text{grad } U = -\nabla U(\underline{r}) \quad (8.1)$$

$U(\underline{r})$ is the electrostatic potential (= work). The negative sign results because the potential decreases in field direction.

$$U(P) = -\int_{\infty}^P \underline{E} \cdot d\underline{s}$$

is then the work to bring a positive unit charge from ∞ to a point P. From (8.1) follows for the current:

$$\underline{J} = -\sigma \nabla U \quad (8.2)$$

i.e., $\underline{J} \perp U = \text{const.}$, the same holds of course for \underline{E} .

In a source-free region V:

$$\int_A \underline{J} \cdot d\underline{A} = 0 \quad ,$$

or, in words, the same amount flows out of a plane as enters. With Gauss' theorem

$$\int_A \underline{J} \cdot d\underline{A} = 0 = \int_V \text{div } \underline{J} dV$$

follows:

$$\text{div } \underline{J} = 0,$$

$$\operatorname{div}(-\sigma \operatorname{grad} U) = 0$$

$$\operatorname{grad} \sigma \cdot \operatorname{grad} U - \sigma \operatorname{div} \operatorname{grad} U = 0 \quad .$$

Because $\operatorname{div} \operatorname{grad} U = 0$, we arrive at the *Laplace equation*:

$$\nabla^2 U = 0 \tag{8.3}$$

We now consider a point source in a medium, which we may imagine as a sphere with vanishing radius $r_0 \rightarrow 0$. A point electrode is physically of course not realizable, so we think the 2nd electrode to be at infinity and measure also the potential difference against infinity, while defining: $U(\infty) := 0$.

The symmetry of the problems calls for a spherical coordinate system (r, ϑ, φ) as adequate, with a transformation into Cartesian coordinates according to

$$x = r \sin \vartheta \cos \varphi$$

$$y = r \sin \vartheta \sin \varphi$$

$$z = r \cos \vartheta$$

Due to spherical symmetry derivatives to longitude and latitude vanish and the potential U at a point $P(r)$ is solely a function of radius:

$$\frac{\partial}{\partial \vartheta} = \frac{\partial}{\partial \varphi} = 0 \rightarrow U = U(r)$$

Then Laplace's equation reads in spherical coordinates:

$$\nabla^2 U = \frac{\partial^2 U}{\partial r^2} + \frac{2}{r} \frac{\partial U}{\partial r} = 0$$

$$\rightarrow \frac{\partial}{\partial r} \left(r^2 \frac{\partial U}{\partial r} \right) = 0$$

$$\rightarrow \frac{\partial U}{\partial r} = \frac{C_1}{r^2}$$

Integration yields

$$U(r) = -\frac{C_1}{r} + C_2$$

As defined the potential vanishes at infinity

$$\lim_{r \rightarrow \infty} (U(r)) \rightarrow 0$$

and therefore also the integration constant $C_2 = 0$.

The current I with density \underline{J} flows outwards radial-symmetrically. The total current through a sphere with radius r_0 is then

$$\begin{aligned}
I &= 4\pi r_0^2 J = -4\pi \sigma r_0^2 \nabla U \\
I &= -4\pi \sigma r_0^2 \left(\frac{\partial U}{\partial r} \right)_{r=r_0} = -4\pi \sigma r_0^2 \frac{C_1}{r_0^2} \\
\rightarrow C_1 &= -\frac{\rho I}{4\pi} \\
\rightarrow U(r) &= \frac{\rho I}{4\pi r}
\end{aligned} \tag{8.4a}$$

$$\underline{J} = -\frac{1}{\rho} \frac{\partial U}{\partial r} = \frac{I}{4\pi r^2} \frac{\underline{r}}{r} \tag{8.4b}$$

The equipotential lines are orthogonal to the (point-symmetric) current lines, $U = \text{const.}$ is the surface of a sphere with $r = \text{const.}$ The 2nd electrode, which we think to be located at infinity, has no influence on the field in P.

So far we have dealt with a point source in a full space. In order to treat a point source at the surface of a homogeneous half space, we first need to introduce *boundary conditions* at the layer boundaries¹:

1) The potential (and the tangential E-field, too) pass the boundary continuously:

$$U_0 = U_1, \quad E_{t0} = E_{t1} \tag{8.5a,b}$$

If (8.5a) would not be valid, thus $U_0 - U_1 = \delta U \neq 0$, then – because of $\partial U / \partial x \rightarrow \infty$ (since $\partial x \rightarrow 0$) – and it would follow with (8.2) $J \rightarrow \infty$, which is of course nonsense. Correspondingly one proves the continuity of the tangential component of the electric field:

$$\begin{aligned}
\underline{E} &= -\nabla U \rightarrow \nabla \times \underline{E} = 0 \\
\rightarrow \oint \underline{E} \cdot d\underline{s} &= 0 \\
\oint \underline{E} \cdot d\underline{s} &= \int_{K_1} + \int_{K_2} + \int_{K_3} + \int_{K_4} = 0 \\
\rightarrow \int_{K_1} &= -\int_{K_2} \\
\rightarrow E_{t0} &= E_{t1}
\end{aligned}$$

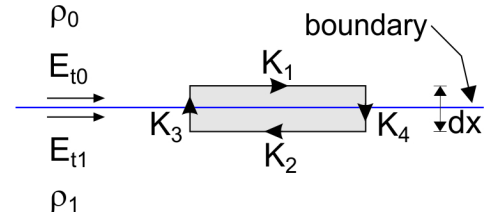


Fig. 8.1: Continuity of the tangential E-field.

2) The normal component of \underline{J} is continuous, while the normal component of \underline{E} jumps invers proportionally to the ratio of conductivities which follows from $\text{div } \underline{J} = 0$.

$$J_{n0} = J_{n1} \tag{8.5c}$$

$$\begin{aligned}
\sigma_0 E_{n0} &= \sigma_1 E_{n1} \\
\rightarrow \frac{E_{n0}}{E_{n1}} &= \frac{\sigma_1}{\sigma_0} = \frac{\rho_0}{\rho_1}
\end{aligned} \tag{8.6}$$

For a point source at the surface of a half space the potential U in spherical coordinates is:

$$U(r) = -\frac{C_1}{r}.$$

¹ More on boundary conditions is found in chapter 5.

Conductivity of the air space near the surface is $\sigma_0 \approx 10^{-14}$ S/m and we simply set it to 0. From the first boundary condition (J_n is continuous through $z = 0$) it follows for $z = 0$:

$$\sigma_0 \left(\frac{\partial U}{\partial z} \right)_{z=-0} = \sigma \left(\frac{\partial U}{\partial z} \right)_{z=+0} = 0 \quad .$$

But also $\partial U / \partial z$ vanishes:

$$\frac{\partial U}{\partial z} = \frac{\partial}{\partial z} \left(-\frac{C_1}{r} \right) = -\frac{\partial}{\partial r} \left(\frac{C_1}{r} \right) \frac{\partial r}{\partial z} = \frac{C_1}{r^2} \frac{2z}{2r} = 0 \quad .$$

Then the current into the air = 0, as it is supposed to be. The total current I through the half sphere is then:

$$I = 2\pi r_0^2 \underline{J} = -2\pi r_0^2 \frac{1}{\rho} \left(\frac{\partial U}{\partial r} \right)_{r=r_0} = -2\pi r_0^2 \frac{1}{\rho} \frac{C_1}{r_0^2}$$

$$\rightarrow C_1 = -\frac{I\rho}{2\pi}$$

and thus the potential:

$$U(r) = \frac{I\rho}{2\pi r} \quad (8.7)$$

The equipotential surfaces are now half sphere surfaces with $\partial U / \partial z = 0$ for $z = 0$ with $U \perp$ surface in $z = 0$ (Fig. 8.2).

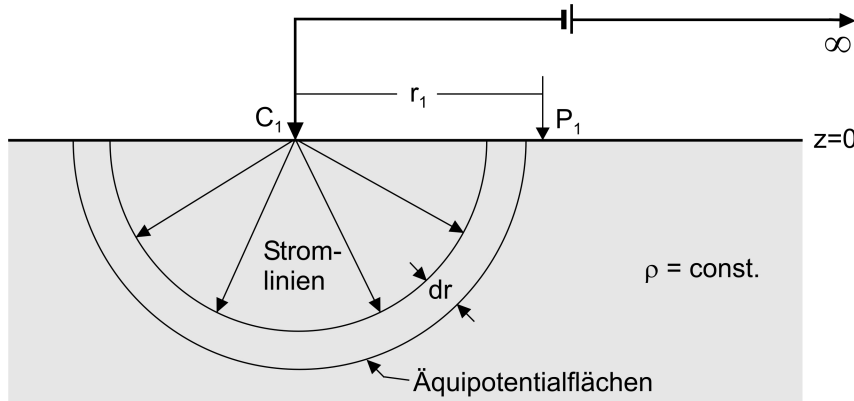


Fig 8.2: Current distribution in a homogeneous half space for injection by a point electrode; the 2nd electrode is thought at infinity.

The current distribution for a 2-point layout is schematically shown in Fig. 8.3; like the potential it is symmetrical around the midpoint of the injection points A and B.

The potential at a point P is now simply the sum of the parts originating from injection points A and B, and, because the current flows into the ground at A (source), and out of the ground at B (sink), the potential of B gets a negative sign:

$$U(P) = U_1(P) + U_2(P) = \frac{\rho I}{2\pi r_1} + \left(-\frac{\rho I}{2\pi r_2} \right) = \frac{\rho I}{2\pi} \left(\frac{1}{r_1} - \frac{1}{r_2} \right) \quad (8.8)$$

Thus resistivity of the half space is determined through measurements of U and I .

As is immediately seen from Fig. 8.3, the current system reaches greater depth with enlargement of the electrode separation (and larger dimensions laterally); Fig. 8.3 shows current and equipotential lines in plane and depth view.

To calculate how much current flows at a certain depth we'll look at the equipotential surface where the potential is identical to zero. Obviously this is the surface where $r_1 = r_2$, the vertical plane between the injection points A and B. On points of this plane the electrical field vector and thus the current density have a component only in x-direction, thus $J_x = \sigma E_x$ and because of $E_x = -\partial U / \partial x$: $J_x = -\sigma \partial U / \partial x$. If we replace now the potential U by the expression in (8.8), we obtain:

$$J_x = -\frac{I}{2\pi} \frac{\partial}{\partial x} \left(\frac{1}{r_1} - \frac{1}{r_2} \right) \quad . \quad (8.9)$$

The distances r_1 and r_2 are now calculated as $r_1 = (x^2 + z^2)^{1/2}$ and $r_2 = ((x-L)^2 + z^2)^{1/2}$, respectively – the dependence on the y-coordinate has been omitted, i.e., we look at $y = 0$ for the midpoint between A and B. Inserting into (8.9) and derivation to x yields:

$$J_x = \frac{I}{2\pi} \left(\frac{x}{(x^2 + z^2)^{3/2}} - \frac{x-L}{((x-L)^2 + z^2)^{3/2}} \right)$$

and for $x = L/2$:

$$J_x = J_x(z) = \frac{I}{2\pi} \left(\frac{L}{(L^2/4 + z^2)^{3/2}} \right) \quad .$$

The ratio of current density $J_x(z)$ at depth z to current density at the surface $z = 0$ is then:

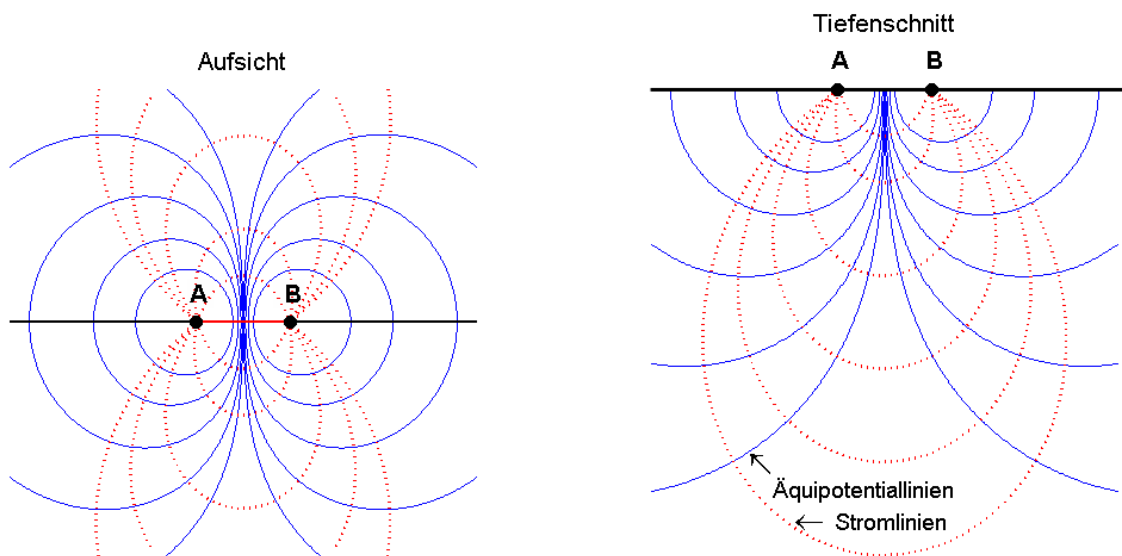


Fig. 8.3: Current distribution and equipotential planes for two point electrodes with a distance $L = \overline{AB} = \overline{C_1 C_2}$.

$$J_f = \frac{J_x(z)}{J_x(0)} = \frac{1}{\left(1 + (2z/L)^2\right)^{3/2}} \quad (8.9b)$$

The portion of the total current is obtained by integration of (8.9b):

$$\begin{aligned} I_f &= \frac{2}{\pi} \arctan \left(\frac{z}{L/2} \right) \\ &= \frac{2}{\pi} \arctan \left(\frac{2z}{L} \right) \end{aligned} \quad (8.9c)$$

Thus above $z = L/2$ flows half of the total current $I_f = 0.5$ (see Fig. 8.4). This is the quintessence of *geoelectric deep sounding*: By extending the electrode separation we achieve information about resistivity at subsequent larger depth.

In practice such a 2-point layout is useless, however, as the auxiliary circuit diagram in Fig. 8.5 demonstrates. Here R_E denotes the ohmic resistance of the subsoil, R_A and R_B are the *transitional* or *contact resistances* of the electrodes. In the 2-point circuit (dotted line) the measured voltage drop is $U \sim (R_A + R_E + R_B)$. These contact resistances are caused by insufficient contact of the electrodes (e.g., steel rods) with the ground and eventual oxidation layers; they stay principally unknown and adulterate the wished result, namely the determination of earth resistance R_E for certain electrode geometry². A solution of this problem is obtained by a separate circuit to measure the voltage (continuous line in Fig. 8.5). The measurement should be "current-less", i.e., the inner resistance of the voltmeter or amplifier should be as high as possible.

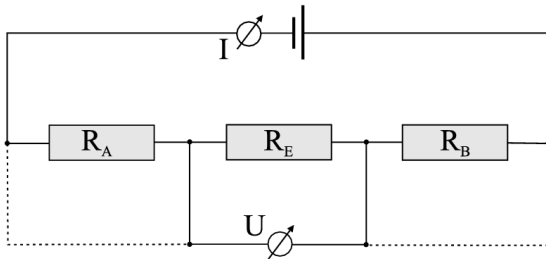


Fig. 8.5: Auxiliary circuit diagram for 2- and 4-point configuration.

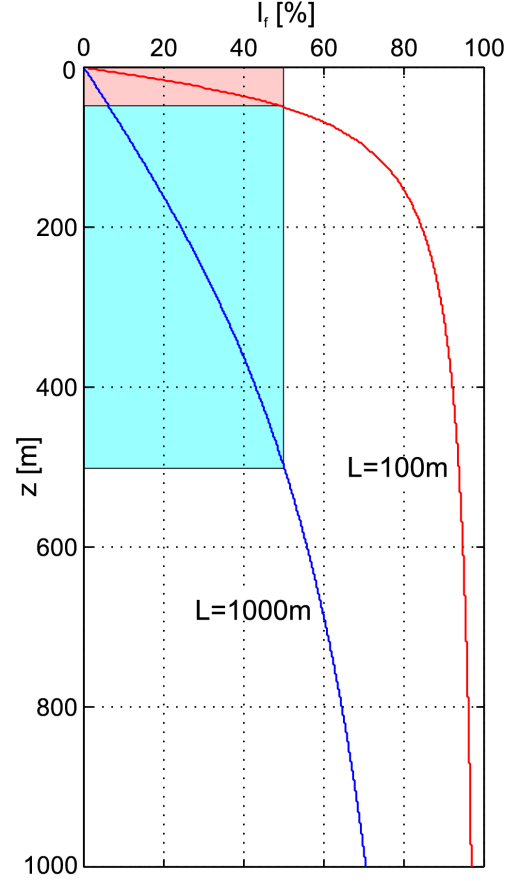


Fig. 8.4: Portion of the current system in %, which flows above a depth z , plotted for electrode separations of $L=100m$ and $L=1000m$.

The simple expressions for the 2-point array have thus to be extended in the sense that the potential at a second location has to be taken into account (see Fig. 8.6):

$$\begin{aligned} U(M) &= \frac{\rho I}{2\pi} \left(\frac{1}{r_1} - \frac{1}{r_2} \right), \\ U(N) &= \frac{\rho I}{2\pi} \left(\frac{1}{r_3} - \frac{1}{r_4} \right) \end{aligned}$$

² Keyword coupling: In practice the resistance between the current electrodes (thus $R_{ges} = R_A + R_E + R_B$) should be in the order of not more than a few $k\Omega$; a higher resistance results in a smaller current flow I , which impedes an exact voltage measurement. The inner resistance of modern voltmeters is in the order of $G\Omega$, but unfortunately this is often not realized in commercial instruments. Usage of geoelectrics is thus limited in desert areas.

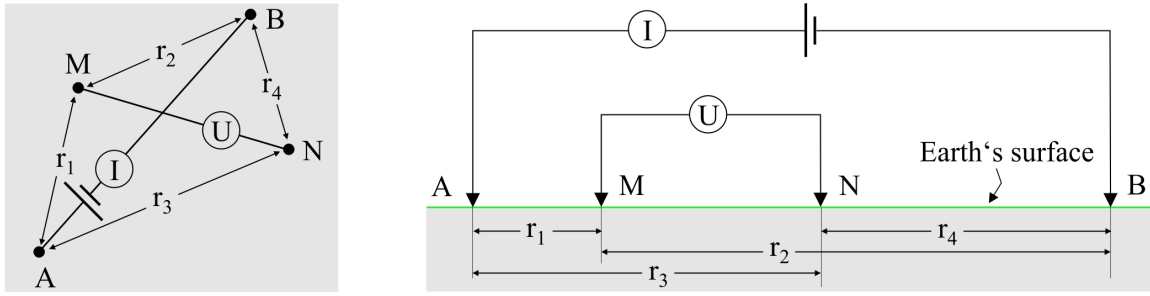


Fig. 8.6: Derivation of potentials in a 4-point layout, to the left in arbitrary configuration on a plane, to the right layout on a straight line.

It follows for the potential difference (= voltage) between M and N:

$$\Delta U = U(M) - U(N) = \frac{\rho I}{2\pi} \left(\frac{1}{r_1} - \frac{1}{r_2} - \frac{1}{r_3} + \frac{1}{r_4} \right) \quad (8.10)$$

By measuring ΔU and I and with known distances $r_1 - r_4$ (measuring tape!) we obtain:

$$\rho = \frac{2\pi \Delta U}{I} \left(\frac{1}{r_1} - \frac{1}{r_2} - \frac{1}{r_3} + \frac{1}{r_4} \right)^{-1} = G \frac{\Delta U}{I} \quad (8.11)$$

This is the fundamental equation of geoelectric deep sounding; it is used at least implicitly at every measurement³. G is termed *geometry* or *configuration factor*, measured in m.

Man may of course place the current and voltage dipoles arbitrarily; but one usually arranges electrodes and probes more conveniently in a symmetric manner. The most common configurations are displayed in Fig. 8.7. They each have specific advantages and disadvantages with respect to measuring effort and accuracy, i.e., the signal-to-noise ratio. For the configurations in Fig. 8.7 we get the following geometry factors:

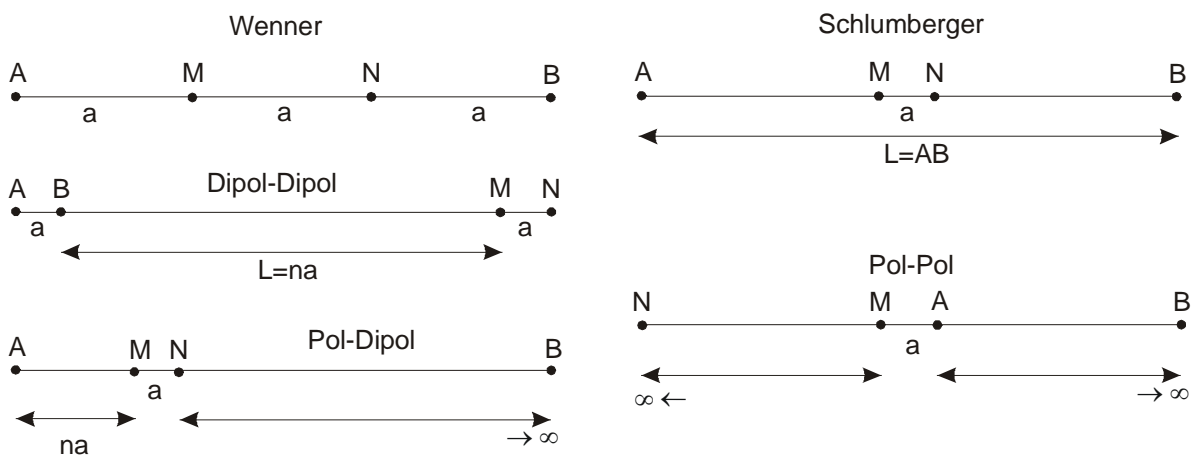


Fig. 8.7: Common 4-point layout of DC resistivity. For the Pole-Dipole spread other variants are used as well.

³ It makes by the way no difference if the current is fed through (M,N) and the voltage is measured at (A,B); the ratio voltage/current and thus the derived resistivity stay the same (principle of *reciprocity*, see Parasnis 1988).

$$\begin{aligned}
\text{Wenner } (\alpha): & \quad G = 2\pi a \\
\text{Schlumberger:} & \quad G = \frac{\pi}{a} \left[(L/2)^2 - (a/2)^2 \right] \text{ oder } G = \frac{\pi}{a} \left[(L/2)^2 \right] \text{ für } L \gg a \\
\text{Dipole-Dipole:} & \quad G = \pi n(n+1)(n+2)a \\
\text{Pole-Pole:} & \quad G = 2\pi a \\
\text{Pole-Dipole:} & \quad G = 2\pi n(n+1)a \quad (n > 3)
\end{aligned} \tag{8.12a-f}$$

The latter configuration is also termed Half-Schlumberger-, Hummel- or Three-Pole configuration, the Pole-Pole array also Two-Pole.

As defined, the resistivity obtained with eq. (8.11) is independent from the choice of configuration (which means that current and voltage "adjust" themselves accordingly). If we look at the general case of a non-homogeneous and/or anisotropic half space, however, we still use eq. (8.11), but now one can only determine an *apparent resistivity* ρ_a . It is a function of electrode/probe spacing, particularly the separation $L = \overline{AB}$ (as such or as function of $L/2$ it is commonly displayed for the Schlumberger array because this reflects the depth dependence of the current systems as shown above):

$$\rho_a = \rho_a(G) = \rho_a(L) \quad . \tag{8.13}$$

Some practical remarks shall be made at this point: to measure the potential difference δU (which is usually in the range of several mV) non-polarizable probes should be employed. Fig. 8.9 shows the principle layout of a Cu/CuSO₄ probe. Other metal/salt combinations are Ag/AgCl or Pb/PbCl, which are more stable in time but also more expensive. The membrane which enables the electric contact to the ground should be chosen in a way that it only enables a minimum fluid interaction. A probe of this kind is mandatory for self-potential and also MT measurements. In multi-electrode arrays one usually abstains from non-polarizable probes for reasons of practicability. For the electrodes, steel or brass stakes are usually employed, which have to be bundled and/or watered under poor coupling conditions. Newer developments apply capacitive coupling with injection of alternate current (e.g., OhmMapper by Geometrics).

The injected current is usually in the range of several mA up to several hundred mA; for this one needs voltages in the order of several ten to several hundred V, occasionally even kV (the operators have to take great care that no contacts are touched during the measuring cycle!).



Fig. 8.8: Conrad Schlumberger, one of the pioneers of geoelectric exploration.

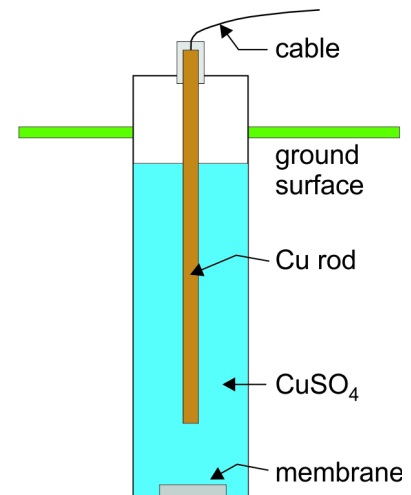


Fig. 8.9: Scheme of a Cu/CuSO₄ probe.

In reality, geoelectrics never uses pure DC current, but rather an alternating current to avoid polarization effects as displayed in Fig. 8.10. An eventual offset of the measured potential may be suppressed this way. The measured voltage often shows a characteristic as in Fig. 8.10, which is the result of charge/polarizing effects in the ground (see IP method later). The measurement interval may thus start only after this relaxation phase.

Apparent resistivity as function of electrode separation is plotted in a double-logarithmic diagram, thus $\log_{10}(\rho_a) - \log_{10}(L/2)$. Separations $L/2$ should be chosen logarithmically equidistant, with about 8 points/decade, i.e., according to the scheme $(L/2)_i = 10^{i/8}$ m with $i = 1, \dots, 8, \dots, 16, \dots$. For the Wenner array, $\log_{10}(a)$ is drawn as abscissa.⁴

Sometimes geoelectric devices are designed in a way that the magnitude of the injection current is programmable to fixed values. This may lead to problems when the contact resistances don't allow the feeding of such a current (with limitations of the output voltage); it must be reduced often which in turn leads to a decreased voltage at the probes. By increasing the separation of the potential probes the measured signal is increased; this is an inherent advantage of the Wenner over the Schlumberger array (see Fig. 8.11).

Before the age of computerized inversion (which is done today already in the field for 1-D cases, at least in the sense of an estimation), data were often analyzed with the help of curve atlases. So-called master curves were used, which showed normalized apparent resistivities and electrode spreads for multi-layered subsoil. Fig. 8.12 shows the example of a 2-layer case with ρ_a normalized with ρ_1 and $L/2$ with d_1 (calculation of such curves will be treated later).

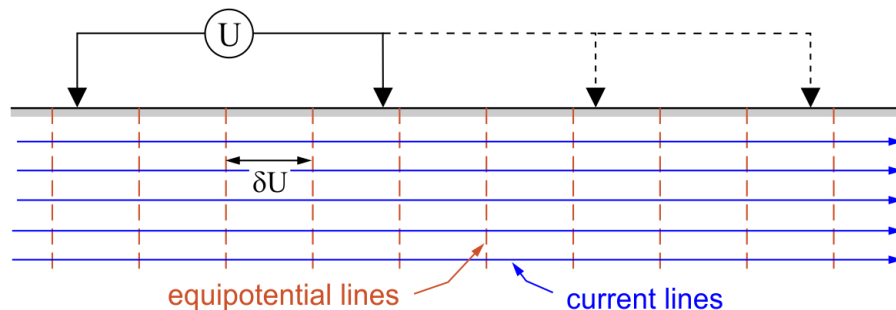


Fig. 8.11: An increased separation of voltage probes leads to an increase of the measured signal. Here we assume a horizontal current flow in a homogeneous or layered medium.

⁴ It is highly recommended to design the double-logarithmic diagram in a way that one decade on the abscissa is exactly as large as a decade on the ordinate (in cm). In commercial software one often finds a condensed display, the curves appear then smoother and of higher quality as they really are.

The parameters at the curves show the resistivity ratio ρ_2/ρ_1 . Data points were plotted on transparent paper and matched with one of the curves; from there one could directly read the model of the subsoil. One may easily imagine the work when interpreting multi-layer cases...

Concerning models of the earth one usually distinguishes between two approaches: the one-dimensional, *layered subsoil* and the case of a two-dimensional *lateral conductivity contrast* (nature is of course far away from these idealizations and more complicated, i.e., three-dimensional and/or anisotropic). Correspondingly we call methods to explore a layered half space *sounding*, those for a laterally inhomogeneous half space *profiling* (see Fig. 8.13).

In a sounding the electrode spread is enlarged successively (with fixed midpoint) in order to reach deeper layers of the subsoil; during profiling the whole array is shifted across the supposed conductivity boundary (with fixed configuration). Under "sounding-profiling" or better *tomography* one understands the combination of both principles with a multi-electrode configuration.

To understand apparent resistivity curves as function of spread or location we first have to further investigate the conditions at the boundary between two homogeneous domains (we skip anisotropy for the time being), i.e. the boundary conditions (8.6a-c):

$$U_1 = U_2 \quad E_{t1} = E_{t2} \quad J_{n1} = J_{n2} \quad (8.14)$$

This is illustrated in Fig. 8.18.

With ϕ_1 as angle of incidence and ϕ_2 as emergent angle, J_n as normal and J_t as tangential component it follows:

$$J_{n1} = J_{n2} = J_n \quad \frac{J_{t1}}{J_n} = \tan \phi_1 \quad \frac{J_{t2}}{J_n} = \tan \phi_2 \quad (8.15)$$

Continuity of the normal component (it's equal on both sides of the boundary) means nothing

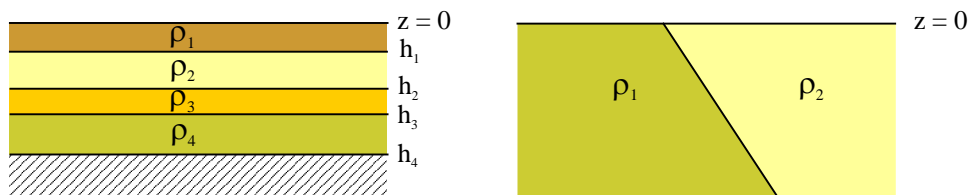


Fig. 8.13: Idealized models of inhomogeneous subsoil. Left: layered half space, right: lateral resistivity contrasts.

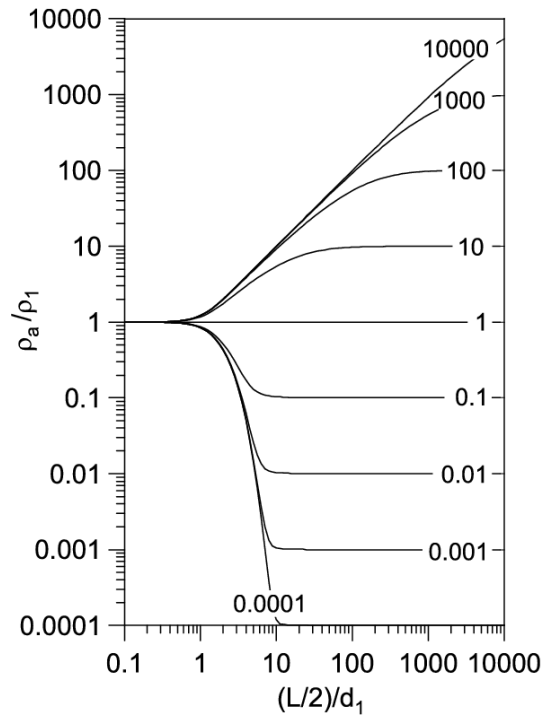


Fig. 8.12: Example of a set of master curves for the 2-layer case.

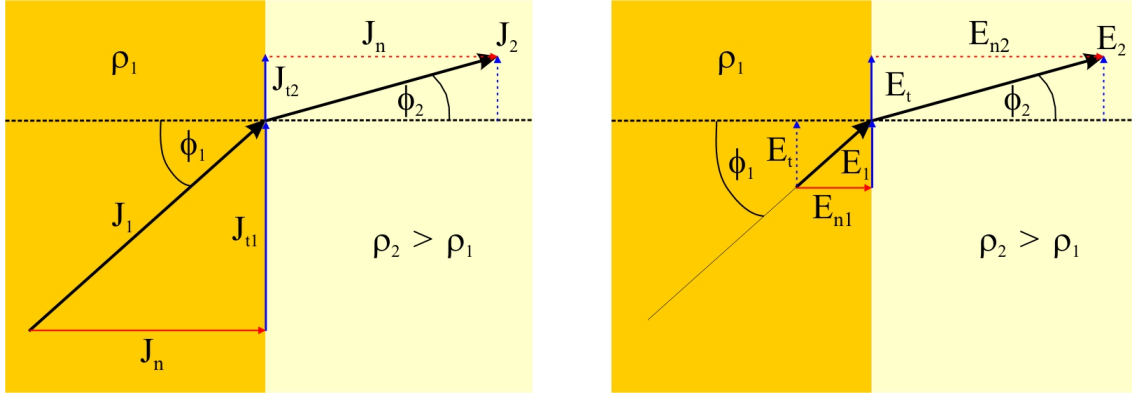


Fig. 8.14: Continuity and jump conditions of current density and electrical field at a boundary.

else than that the current penetrates deeper into the poor conductor.

For the components of the electrical field the opposite holds because of the generalized Ohm's law; the tangential component is continuous, the normal component jumps proportionally to the resistivity contrast:

$$\begin{aligned}
 J_n &= \sigma_1 E_{n1} = \sigma_2 E_{n2} \\
 J_{t1} &= \sigma_1 E_t \\
 J_{t2} &= \sigma_2 E_t \\
 \text{thus } E_t &= \frac{J_{t1}}{\sigma_1} = \frac{J_{t2}}{\sigma_2}
 \end{aligned} \tag{8.16}$$

It follows

$$\frac{J_{t1}}{J_{t2}} = \frac{\sigma_1 E_t}{\sigma_2 E_t}$$

and with (8.16) the law of refraction of the current lines:

$$\frac{\sigma_1}{\sigma_2} = \frac{\rho_2}{\rho_1} = \frac{\tan \phi_1}{\tan \phi_2} \quad . \tag{8.17a}$$

This important law is illustrated again in Fig. 8.15. For the (continuous) normal current density it applies:

$$J_n = J_1 \cos \phi_1 = J_2 \cos \phi_2 \tag{8.17b}$$

and for the (continuous) tangential E-field⁵:

$$E_t = E_1 \sin \phi_1 = E_2 \sin \phi_2 \quad , \tag{8.17c}$$

from which follows again (8.17a) because of

⁵ This is Snell's law of refraction.

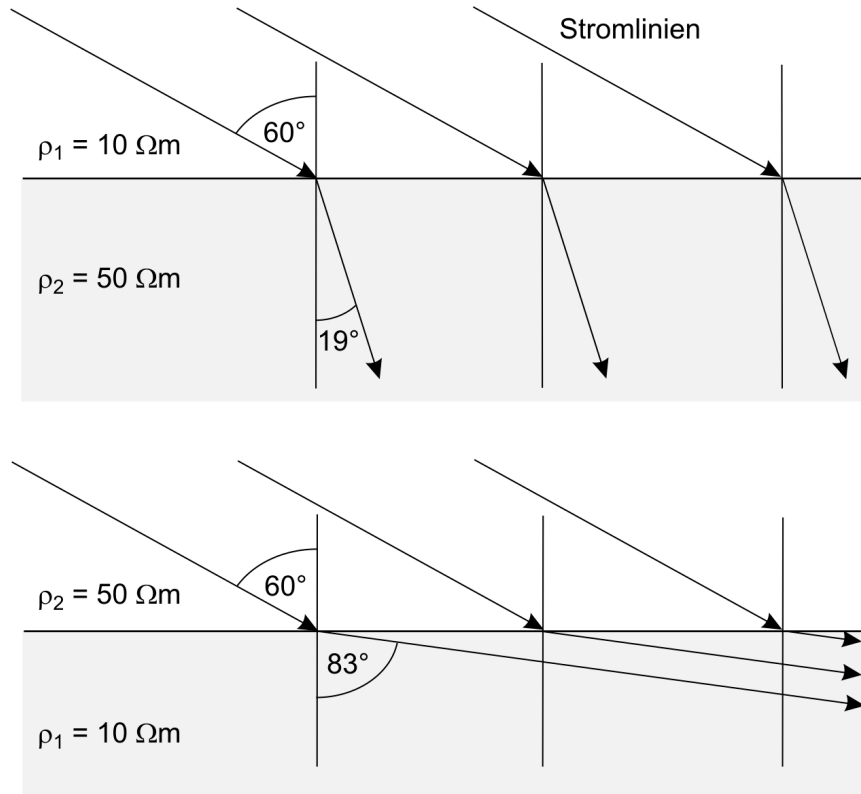


Fig. 8.15: Refraction of current lines at a boundary, the angle of incidence is each time 60° . Above: Poor conductor beneath good conductor, the refraction angle is 19° and the current lines penetrate deeper into the resistor. Bottom: If the current lines penetrate into a good conductor, a current concentration results at the boundary, the refraction angle is 83° . See eq. (8.16).

$$J_1 = \frac{J_n}{\cos \phi_1} = \sigma_1 E_1 \quad \text{and} \quad J_2 = \frac{J_n}{\cos \phi_2} = \sigma_2 E_2$$

$$\rightarrow \frac{1}{\rho_1} E_1 \cos \phi_1 = \frac{1}{\rho_2} E_2 \cos \phi_2$$

$$\rightarrow \frac{\rho_2}{\rho_1} = \frac{E_2 \cos \phi_2}{E_1 \cos \phi_1} = \frac{\sin \phi_1 \cos \phi_2}{\sin \phi_2 \cos \phi_1} = \frac{\tan \phi_1}{\tan \phi_2}$$

So far we have only looked at the conditions in the immediate surroundings of the boundary (where the current lines may be drawn as straight lines). For the farther environment of the boundary we study the current system with the help of the next figures. Figs. 8.16 and 8.17 illustrate once more the principle of deep sounding and the value of apparent resistivity with successive enlargement of spread L . At small L , ρ_a "sees" only the upper layer, the largest part of the current system flows exclusively above the boundary, therefore $\rho_a = \rho_1$. At intermediate spreads a significant part of the current flows above as well as below the conductivity boundary, therefore now $\rho_1 < \rho_a < \rho_2$. For large L ρ_a sees quasi only the lower layer, hence here we have $\rho_a = \rho_2$.

In Fig. 8.18 exemplary $\rho_a(L/2)$ curves are displayed for the Schlumberger array. One recognizes the asymmetric shape, i.e., the drop for a good conductor beneath a poorly conducting overburden is much stronger than the rise for the opposite case.

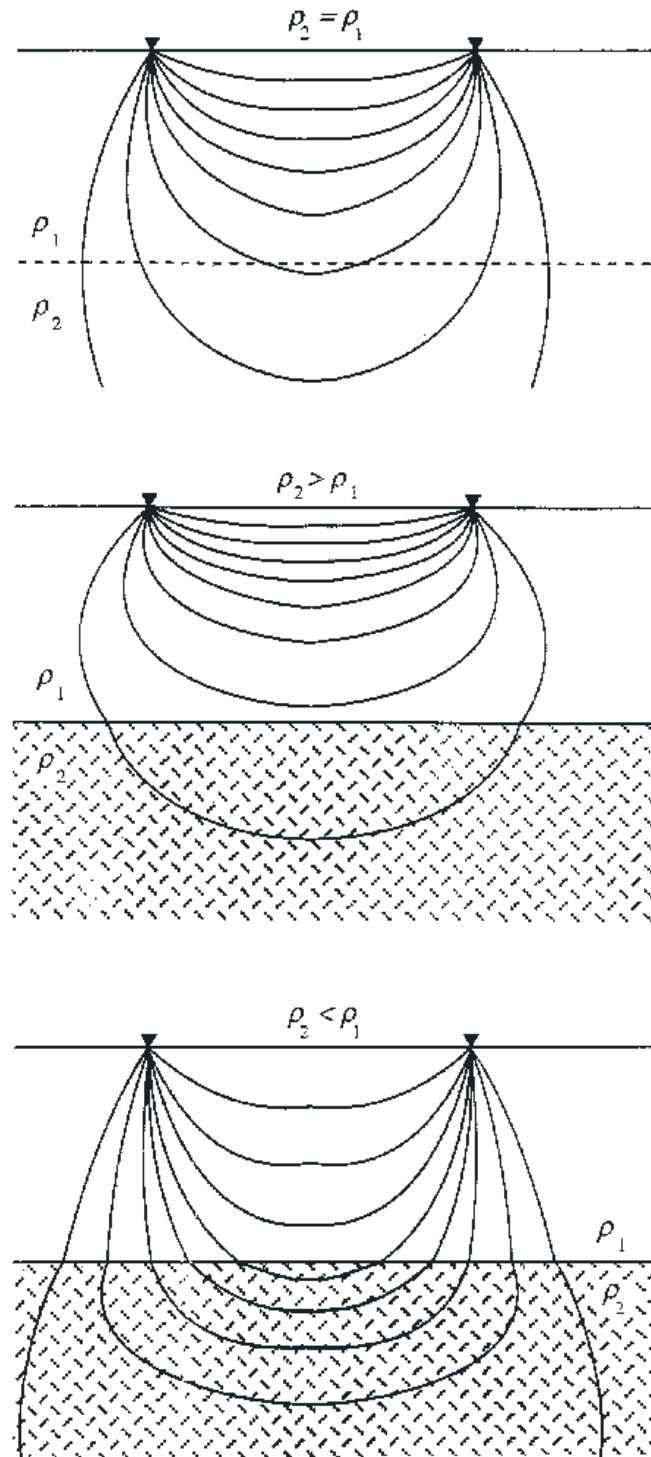


Fig. 8.16: Current system in two-layered subsoil with varying resistivity of the substrate. From P. Kearey, M. Brooks, I. Hill (2002): An introduction into geophysical exploration, Wiley-Blackwell.

In interpreting ρ_a curves we have to consider that the geoelectric problem is indeed in large parts unique, i.e., small changes of the model parameters (layer resistivities and thicknesses) cause distinguishable variations of the model response. However, in certain limits, changes of the model response may be so small that the different models may not be distinguished within certain error intervals (a measured ρ_a curve is rarely fitted to better than approx. 1%). De-

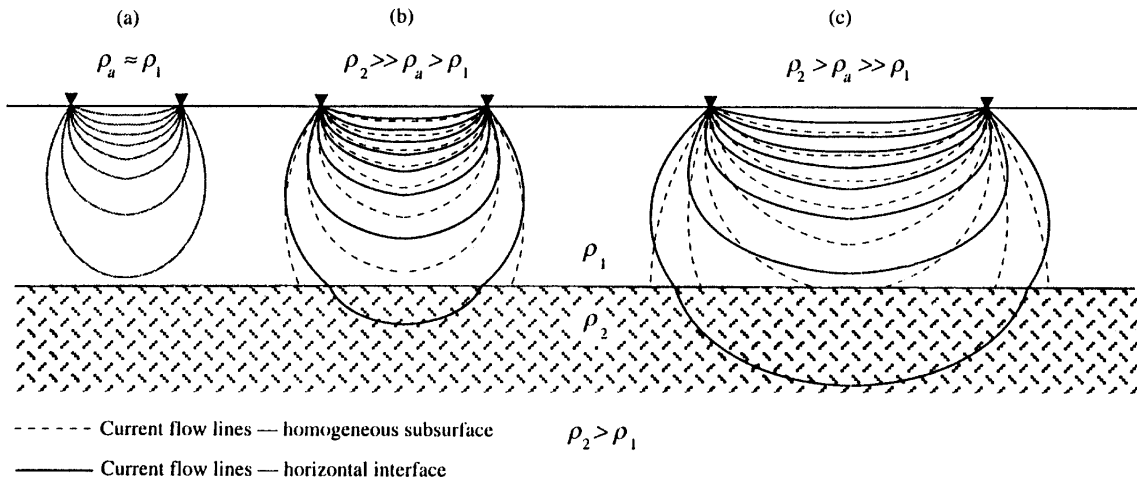


Fig. 8.17: Current system and apparent resistivity for a 2-layer case when the spread is expanded.

pendent on curve type one speaks of the *principle of equivalence* or of *layer suppression*, respectively.

For equivalent models 2 cases have to be distinguished: If there is – in a 3-layer case – a well-conducting layer interbedded between two resistive layers, perhaps only the *conductance* (conductivity-thickness product) of this layer may be resolved:

$$\tau_2 = \sigma_2 d_2 = d_2 / \rho_2 .$$

In literature this is often termed τ - or S-equivalence (see Fig. 8.19); if the intermediate layer is more resistive than the overburden and the substrate, only the *transversal resistivity* will be resolved from the ρ_a curves:

$$T_2 = \rho_2 d_2 \quad \text{with} \quad [T] = \Omega \text{m}^2 .$$

If one varies ρ_2 and d_2 within certain limits in a way that the resulting conductance or trans-

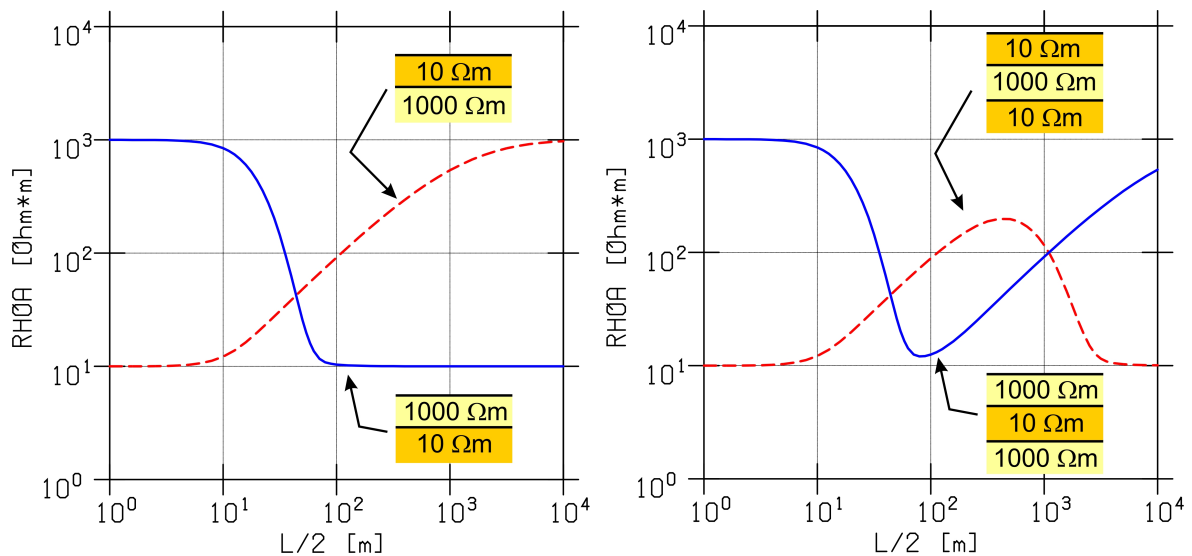


Fig. 8.18: ρ_a curves for 2- (left) and 3-layer (right) cases for a Schlumberger array. Layer thicknesses are 10 m for the overburden and 100 m for the intermediate layer on the right hand side.

versal resistivity stays the same, the corresponding response does not change within the error bounds.

The phenomenon of layer suppression may occur when the resistivity of the intermediate layer lies between the overburden and the substrate:

$$\rho_1 < \rho_2 < \rho_3 \quad \text{or} \quad \rho_1 > \rho_2 > \rho_3 \quad .$$

Again, ρ_2 and d_2 may vary within certain limits without having a significant effect on the model response.

Both non-unique cases are of course not restricted to 3-layer cases; also combinations of equivalence and layer suppression are possible.

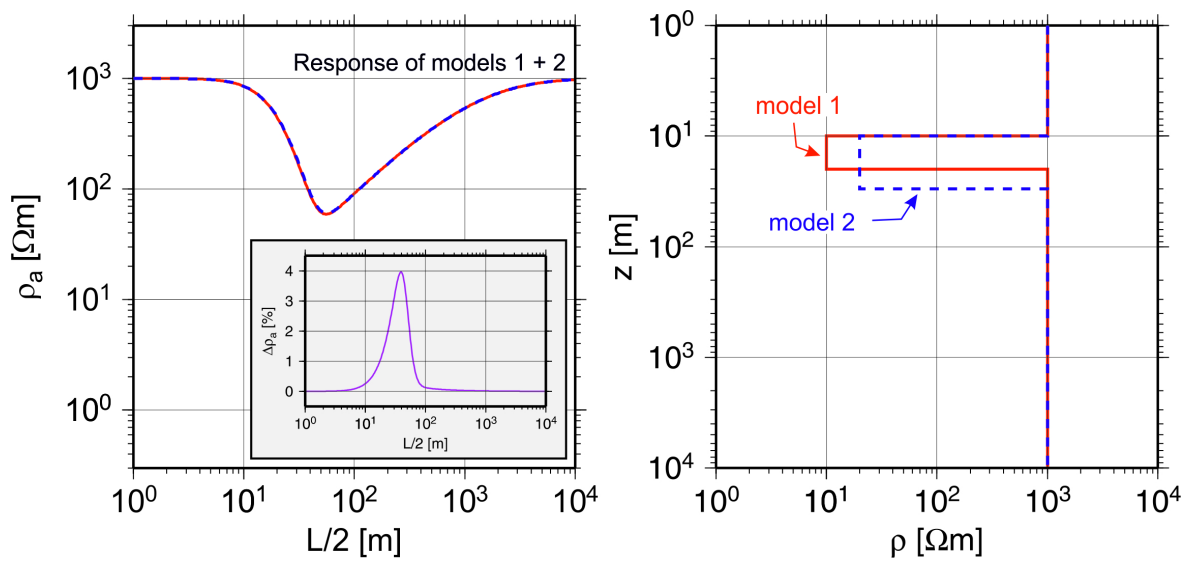


Fig. 8.19a: Model response (left) for two equivalent 3-layer models (right): Model 1: $\rho_2 = 10 \, \Omega\text{m}$, $d_2 = 10 \, \text{m}$; Model 2: $\rho_2 = 20 \, \Omega\text{m}$, $d_2 = 20 \, \text{m}$. Conductance of the 2nd layer is $1 \, \text{S}$ in both cases.

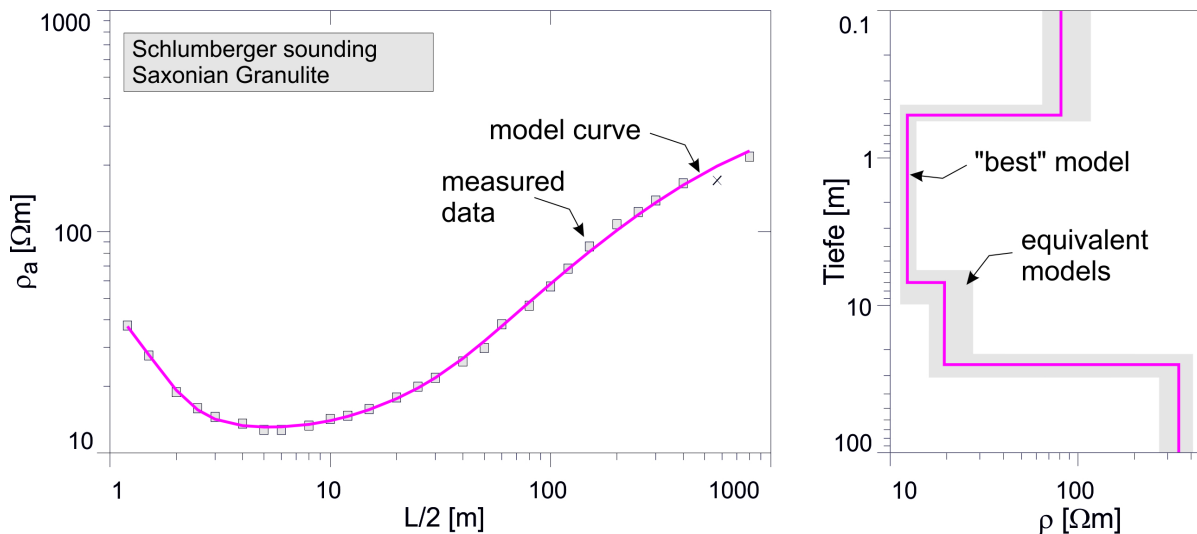


Fig. 8.19b: A practical example: The equivalent models surround the "best" model approximately like an envelope. One recognizes specifically the poor resolution of the second layer boundary.

If lateral variations of conductivity are present in the subsoil (which is indeed the normal case), a deep sounding procedure at a point leads to false results, because, e.g., the influence of an inclined layer in the strike of the spread is not distinguishable from a 1-D curve. Only a cross or circle sounding (Fig. 8.20) would clarify the situation. The standard method to take lateral contrasts into account is "*lateral profiling*", however, where a 4-point array is moved partly or totally above the expected anomaly, holding the electrode/probe separations constant. If the latter are varied, too, one speaks of *sounding-profiling*.

From practical considerations, the Wenner and Schlumberger arrays are both not very useful layouts for profiling as one has to relocate all 4 electrodes/probes together for each measurement. Therefore, dipole-dipole profiling is often applied since only the two probes have to be relocated here. However, a 3-pole configuration may yield a better signal-to-noise ratio and also a better resolution of lateral contrasts, especially at vertical dikes. Fig. 8.21 shows exemplarily for the pole-dipole configuration, how the total array is moved over a contact. Does the contact reach the surface, characteristic discontinuities of the $\rho_a(x)$ -curve are observed for most configurations (not for pole-dipole) depending on which electrode/probe has just past the contact. We skip examples here (see the German manuscript) because today (2011) almost always an integrated approach is employed, combining sounding and profile with one instrument and a multi-electrode configuration.

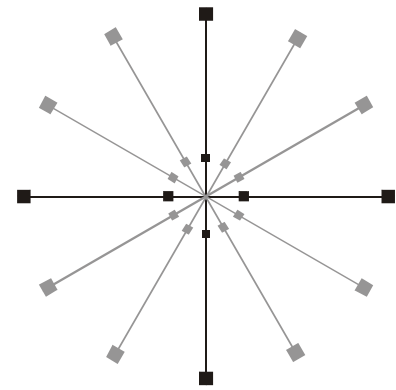


Fig. 8.20: A cross sounding (black lines and electrodes) is complemented and completed by a circle, star or rotational sounding (gray).

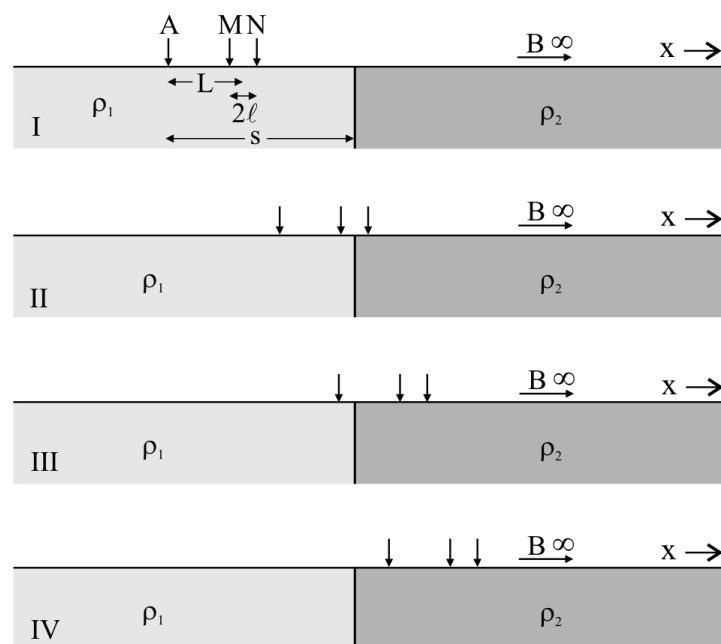


Fig. 8.21: Scheme of profiling over a vertical contact, here with a pole-dipole configuration. The measured $\rho_a(x)$ -values are referred to the midpoint of MN. L is the distance of current electrode A from the midpoint of M and N, 2ℓ is the distance of M and N and s the distance of A from the fault.

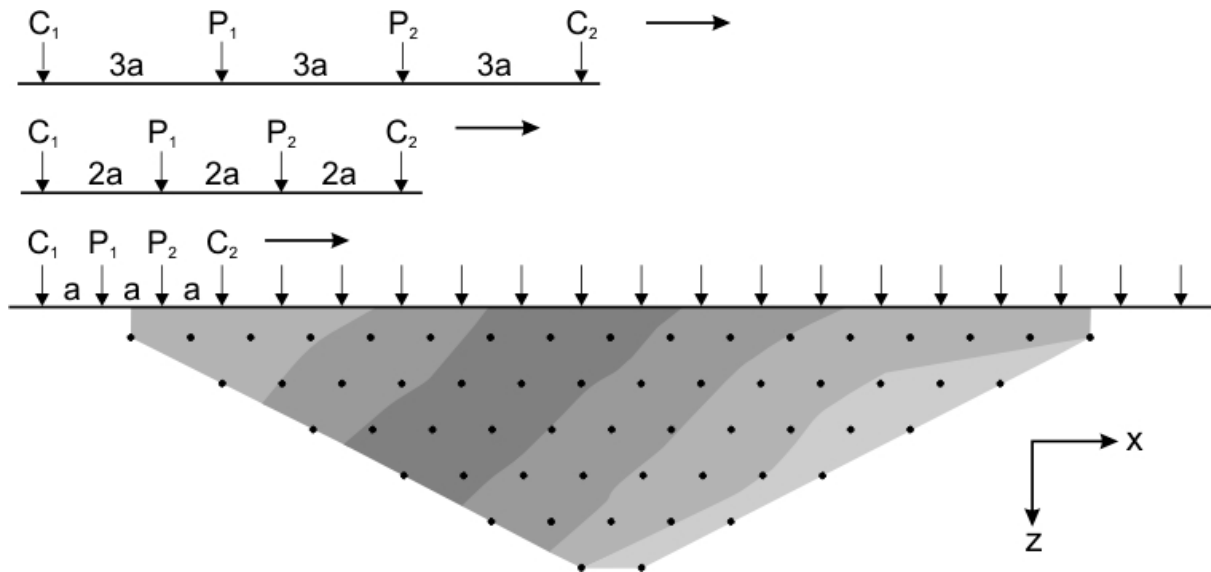


Fig. 8.22: Scheme to construct a geoelectric pseudo section, shown here for a Wenner configuration. The data points – i.e. $\rho_a(x,z)$ – are plotted below the centers of each individual array; depth of these points is proportional to the spread and somehow arbitrary. Through relocation of the arrays (which happens electronically with the help of a computer program after all electrodes have been set and connected) a continuous coverage is achieved. Modern array instruments allow the connection of 64-256 electrodes.

Fig. 8.22 shows schematically how such a combined sounding/profiling yields a *pseudo section* of apparent resistivity vs. lateral location and depth. This methodology is often termed tomography. At this point it shall suffice to give a couple of useful links only: <http://www.geoelectrical.com> and <http://www.resistivity.net>

The following figures give some examples.

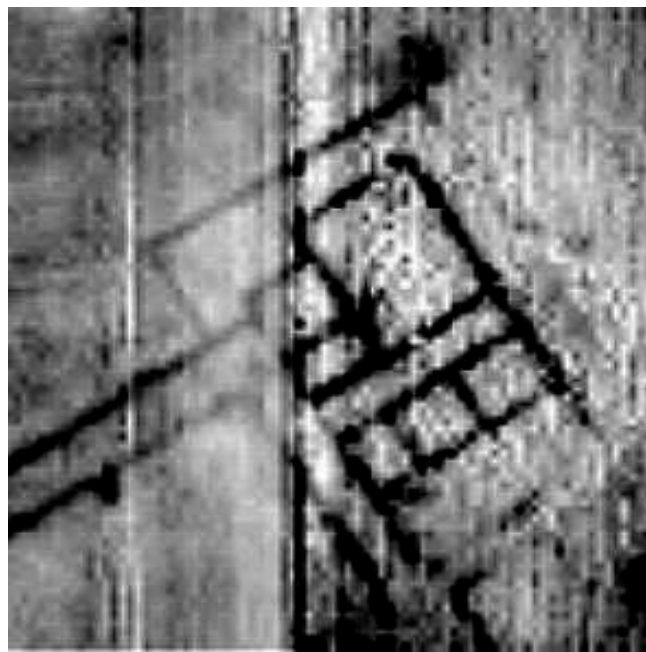


Fig. 8.23: Example of a profiling for the walls of an old Roman villa in Austria (source: web site University of Vienna).

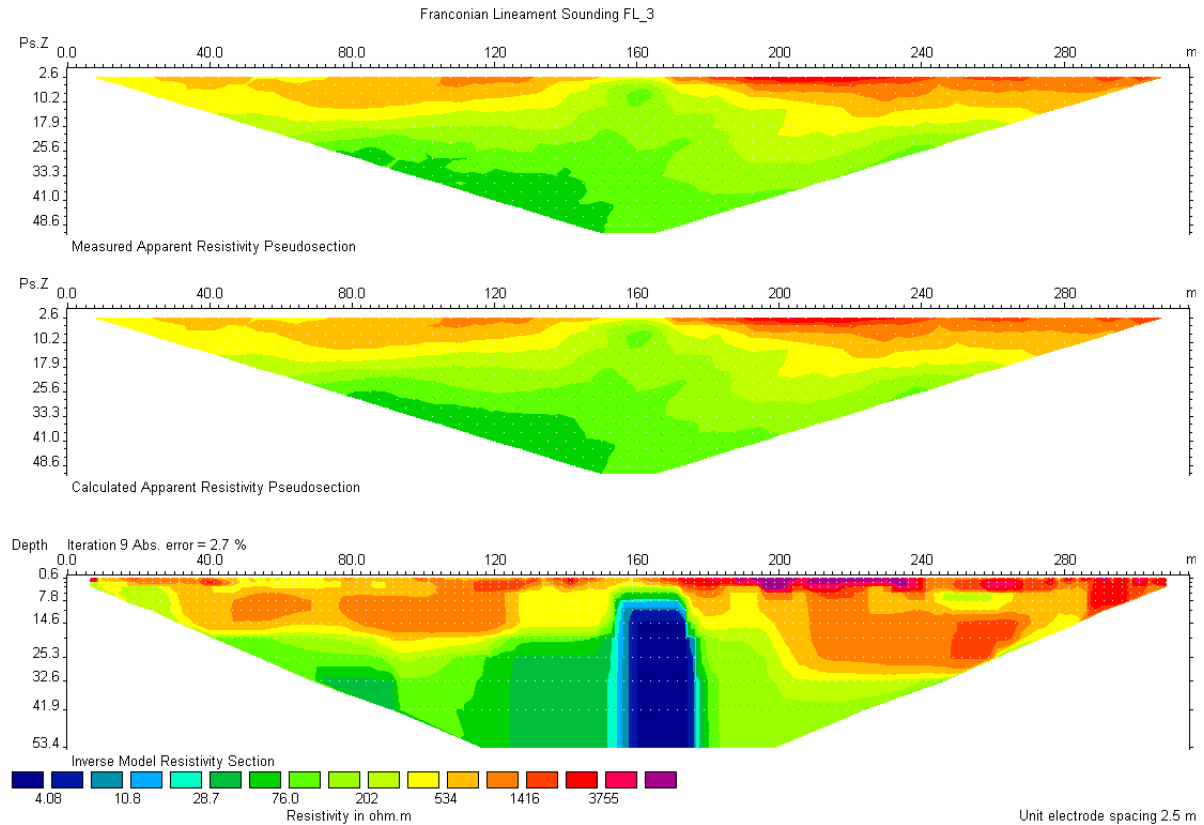


Fig. 8.24: An example of 2-D inversion of data from the Franconian Line in Bavaria, carried out with the program `res2dinv` by Loke and Barker (1996). Top: pseudo section of a Wenner- α measurement, center: model response, bottom: resistivity model. The very good conductor (in blue) is caused by graphitized shear planes, a sub-fault of the Franconian Line system. This conductor is also responsible for a strong self-potential anomaly (see later). Data were collected during a geophysical field excursion of the Free University in 2002.

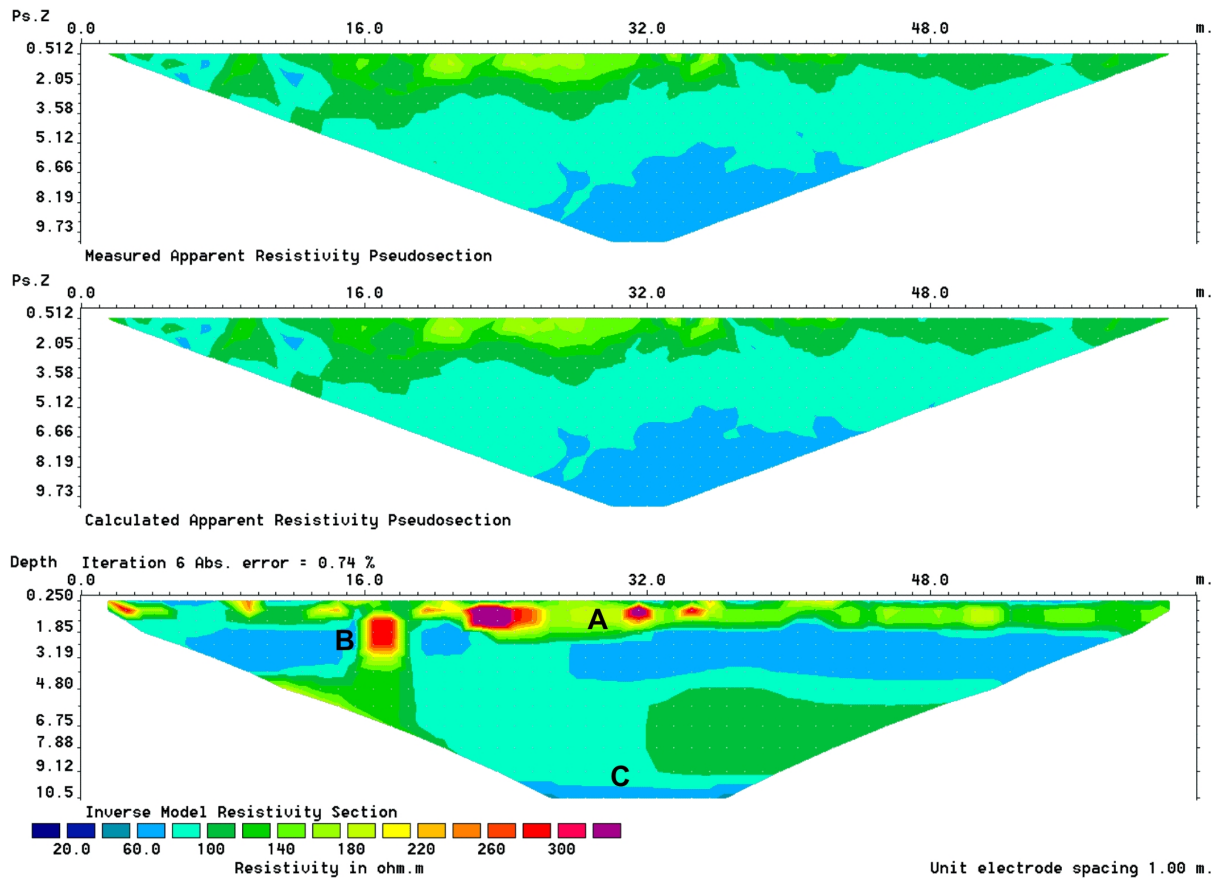


Fig. 8.25: Geoelectric tomography on the sport field of the Free University campus in the district of Lankwitz. A: Near-surface inhomogeneities due to gravel fillings of the field. B: Tunnel from pre-world war II times. C: Aquifer at $z \approx 10\text{m}$ (thus much deeper than downtown). The tunnel, once found could also be accessed directly and its location was determined precisely; due to its small cross section ($\sim 1.40\text{ m}^2$) it's resolved only as a moderately poor conductor. Data were collected during a geophysical practical course in 2004.

9. Self-potential method

In the surrounding of sulfide ore bodies and graphitic zones one discovers frequently a natural electric potential – *spontaneous* or *self-potential* (*SP*) –, which results from the interaction of an electronic (metallic) conductor with oxidizing and reducing environments in the subsoil (*geo-battery*). Other natural potential are often observed at topographic gradients and are due to streaming fluids. It is in this case always negative and may amount to several hundred mV, in special cases even more than 1 V¹. The measuring principle is simply probing the potential difference with the aid of two non-polarizable probes (e.g., based on Cu/CuSO₄ as we have seen in the geoelectrics chapter already) and a voltmeter; this makes it to one of the geoelectrical methods which are easiest to conduct.

Contact- and membrane potentials develop in the presence of electrolytes of different concentration. Let C_1 and C_2 be the electrolyte concentrations, n valence, F Faraday number, R gas constant and T temperature, then the *membrane* or *Nernst potential* is determined as:

$$U_m = -\frac{RT}{nF} \ln \frac{C_1}{C_2} \quad , \quad (9.1)$$

while the *contact* or *diffusion potential* is:

$$U_k = -\frac{v-u}{v+u} \frac{RT}{nF} \ln \frac{C_1}{C_2} \quad . \quad (9.2)$$

Here u and v are the mobility of cations and anions.

If an electrolyte moves in the host rock, *streaming* or *filtration potentials* occur; these have been measured, e.g., at volcanoes at remarkable magnitudes (–3.5 V at Misti volcano in S. Peru, Finizola et al. 2004, see Fig. 9.5 at the end of this chapter). They are calculated from:

$$U_s = \frac{\xi \epsilon \rho}{4\pi \eta} \Delta p \quad (9.3)$$

with Δp = pressure gradient, ξ = electrokinetic potential, ϵ = permittivity, ρ = electrical resistivity and η = dynamic viscosity.

For an SP anomaly to develop at ore bodies it is decisive according to Sato & Mooney (1960) that an electronic conductor intersects domains of different redox potential (Fig. 9.1). Above the groundwater surface the environment is oxidizing (through penetration of atmospheric oxygen), below it is reducing². The redox potential E_H is positive in the oxidation zone, negative in the reduction zone. Are there now – not connected – electronic conductors in the ground, and one measures the potential against a non-polarizable probe close by, the potential difference is identical to zero. However, if one connects these individual bodies through the aquifer top, a compensating electron current will flow in the conductor. In the upper part of the conductor (cathode) electrons pass into the surrounding medium, in the lower part (anode)

¹ The largest SP anomaly known so far, which is due to a metallic body, was encountered with $U = -1.7$ V at an alunite in Cerro de Pasco (Peru).

² As a reminder: Oxidation means loss, reduction gain of electrons. If magnesium is oxidized, for instance, each Mg atom loses both its valence electrons, which are then taken by oxygen: $Mg \rightarrow Mg^{++} + 2e^-$, $O + 2e^- \rightarrow O^{--}$. Oxygen is thus reduced and the total reaction is $Mg + O \rightarrow MgO$.

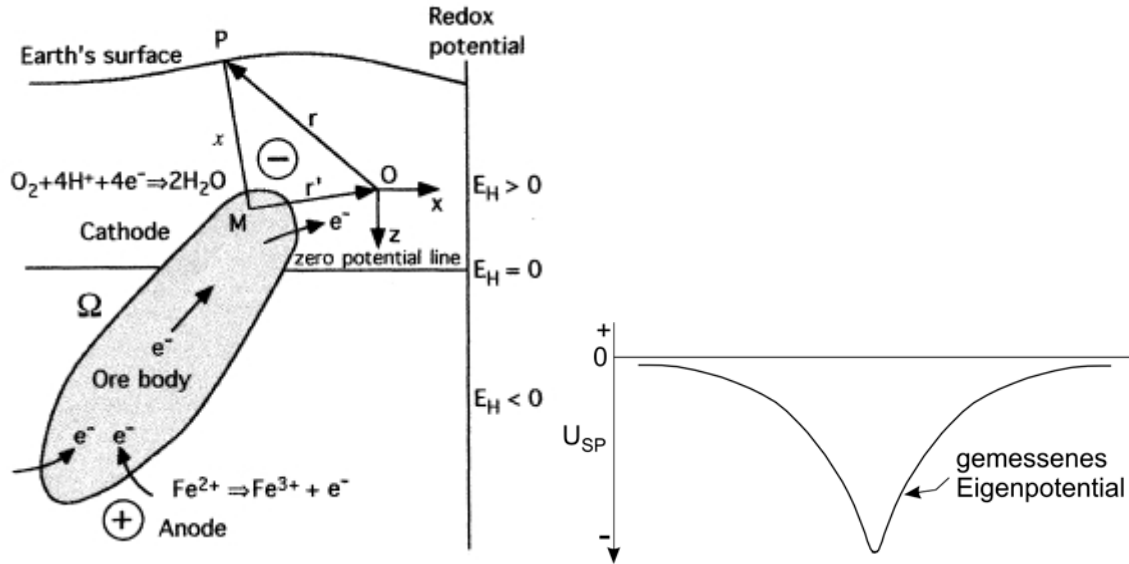


Fig. 9.1: Principle of a geo-battery (Revil et al. 2001) and resulting potential at the surface of the earth, measured against a distant reference (base) probe.

they enter again. At the surface this current is measured as a voltage drop against a distant reference point.

As a simple possibility to interpret measured self-potential anomalies quantitatively one imagines a polarized rod (dipole) in the earth with both ends carrying a "charge" $\pm Q^3$. Let r_1 and r_2 be the distances of these end points to a point P at the surface. Then the potential U at the surface is simply calculated as the sum of both parts:

$$U = \frac{1}{4\pi\epsilon_0} \left(\frac{+Q}{r_1} + \frac{-Q}{r_2} \right) = \frac{Q}{4\pi\epsilon_0} \left(\frac{1}{r_1} - \frac{1}{r_2} \right) \quad (9.1)$$

Because of

$$r_1 = (x^2 + z_1^2)^{1/2} \quad \text{und} \quad r_2 = [(x - a)^2 + z_2^2]^{1/2} \quad ,$$

where $a = L \cos \alpha$ and L is the length of the rod, and α denotes the dip angle (Fig. 9.2), the potential is:

$$U = \frac{Q}{4\pi\epsilon_0} \left\{ \frac{1}{(x^2 + z_1^2)^{1/2}} - \frac{1}{((x - a)^2 + z_2^2)^{1/2}} \right\} \quad (9.3)$$

In realistic modelings, however, the conductivity distribution must be taken into account, which does not work with simple dipole models.

³ Q thus has the unit Coulomb (C = As). This simplistic model does not take conductivity of the surrounding rock into account.

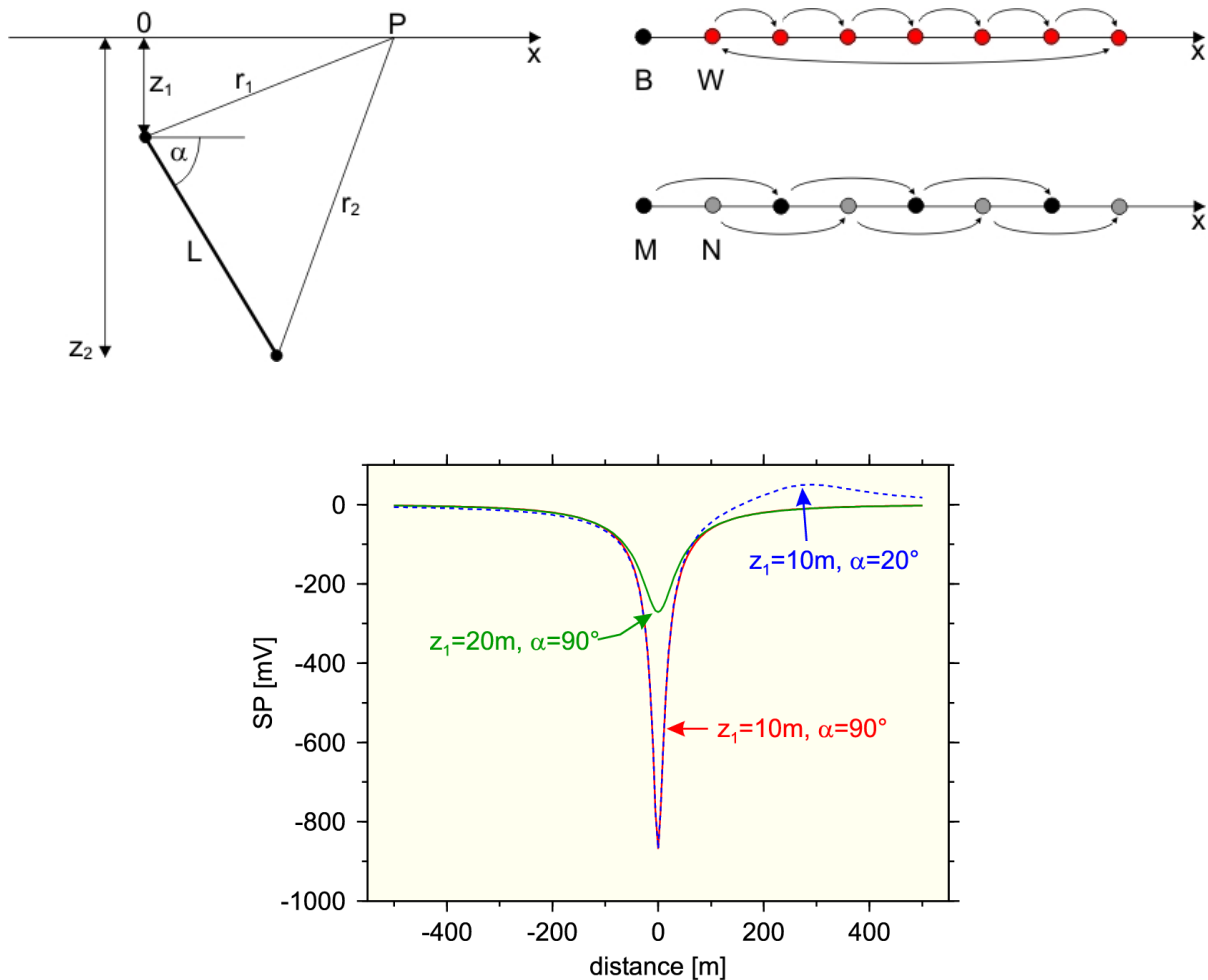


Fig. 9.2: Upper left: Model to explain self-potential anomalies with a polarized rod. Upper right: Layout of a SP profile with base and roaming probe (B, W) and – less common – with mutual relocation of probes M und N ("Leap Frog"). Below the shape of a SP anomaly is plotted exemplarily for different α und z_1 ; the other parameters are unchanged.

In field practice sind, SP measurements belong to the simplest geophysical methods. One only needs a non-polarizable probe (Cu/CuSO₄ suffices) as base, a similar one as roaming probe, cable and a voltmeter with high input resistance. Only with great effort, an accuracy of less than 10 mV may be reached at repeated measurements. This is in the range of telluric variations if the probe separation reaches some hundred meters or more⁴; the temporal drift should thus be corrected for accordingly. From experience it is also difficult to connect different profiles with each other and to find a common, unperturbed reference level. From time to time one observes at hill slopes – caused by streaming potentials – trends of long wavelength or a shift in the reference (null) level.

⁴ In the "Leap-Frog method" both probes are mutually relocated (Fig. 9.2).

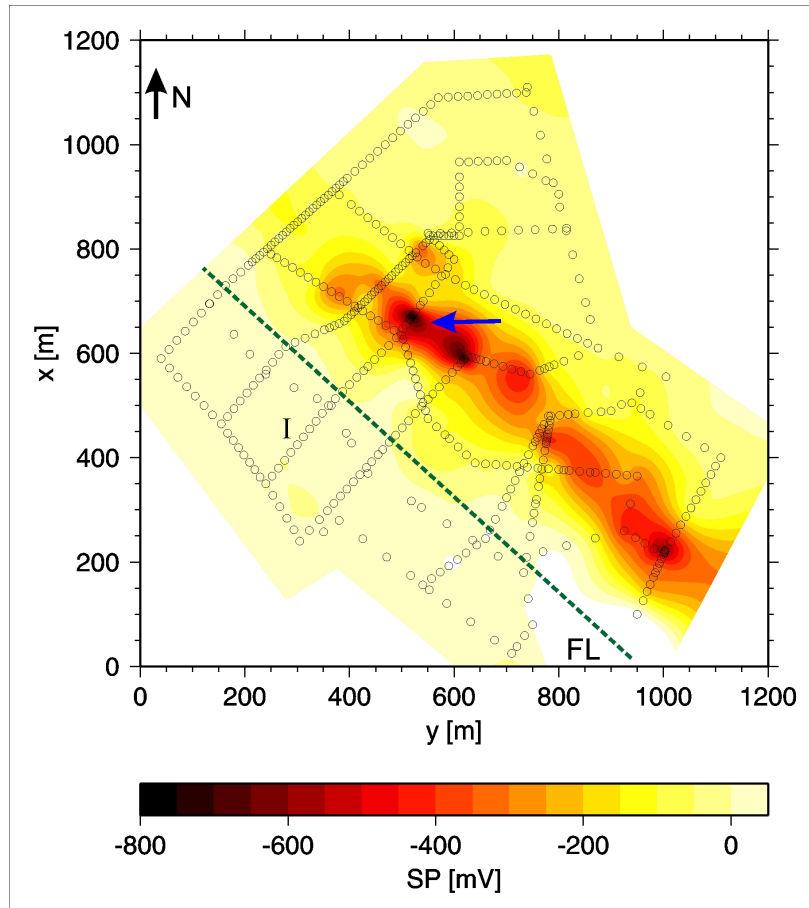


Fig. 9.3: SP anomaly near the Franconian Line in Bavaria, from data collected during a student excursion of the Free University in 1996. The arrow marks the location of a conductivity anomaly which was mapped with DC geoelectrics (see chapter 8).

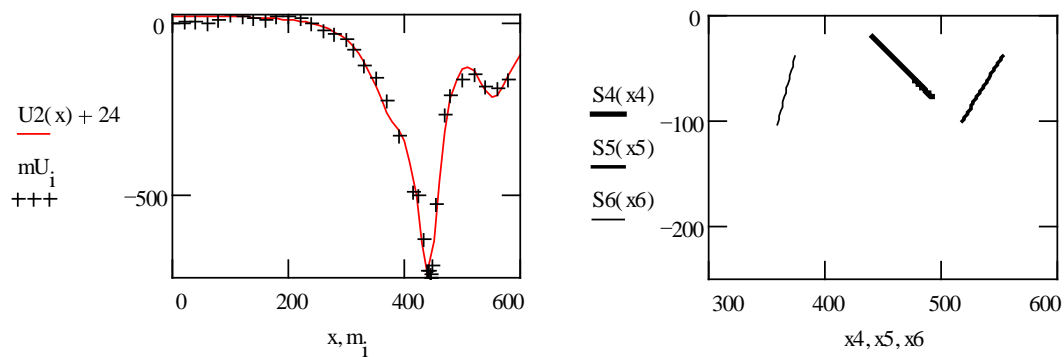


Fig. 9.4: Model calculation for a profile across the central part of the anomaly. It is explained by 3 dipoles of different dip, presumably caused by graphitized shear zones.

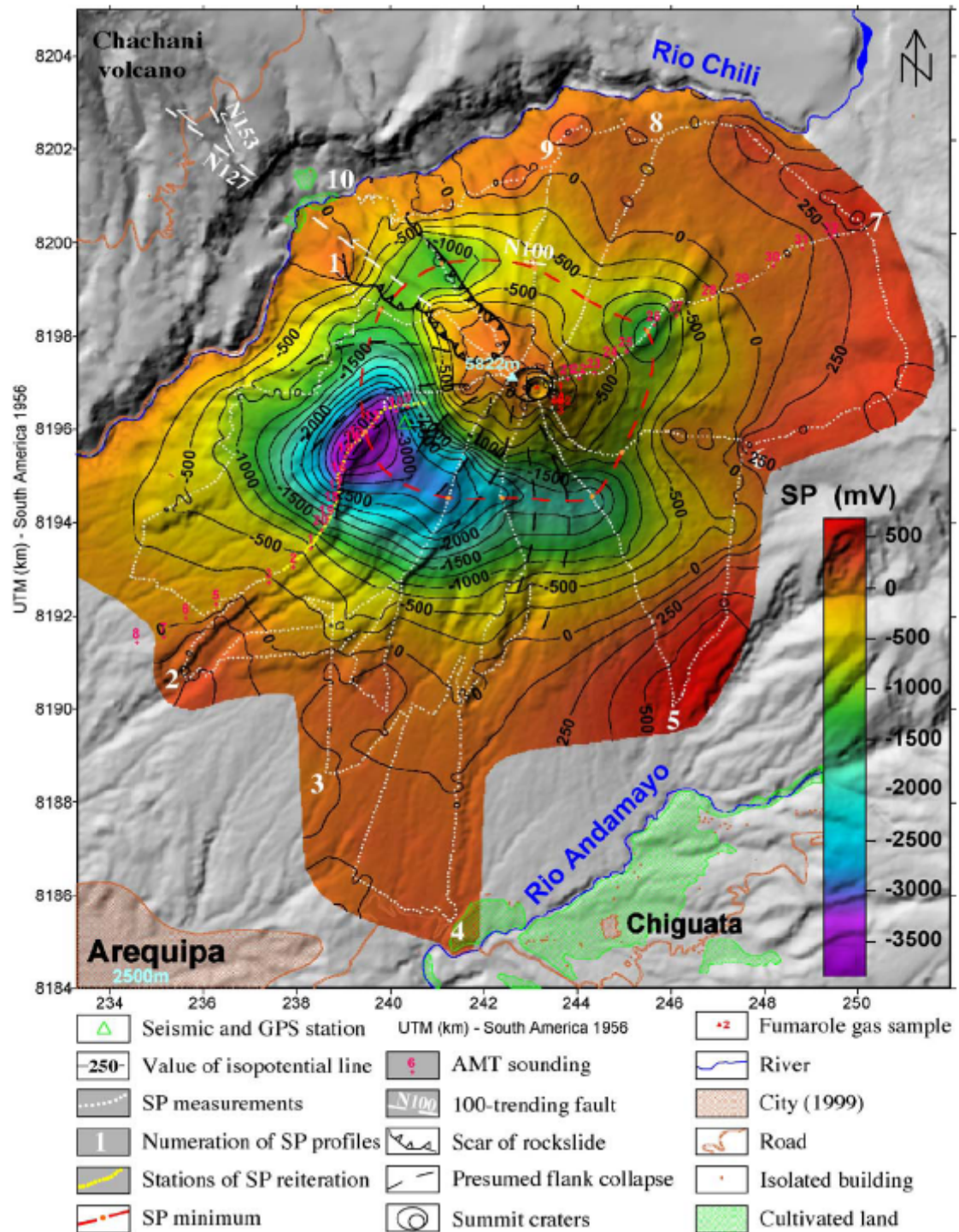


Fig. 9.5: Self-potential at Misti volcano, central Andes, Peru (Finizola et al. 2004). The strong minimum hints a hydrothermal system at the flank of the volcano, which might be relevant for slope stability and safety of the nearby town of Arequipa, Peru's 2nd largest city. A similar anomaly was detected on Mont Fuji, Japan.

10. Induced Polarization (IP)

As was already described in the geoelectrics chapter, the measured voltage of an injected alternating DC current does not follow the current immediately but reaches its maximum (or minimum or zero level) only gradually after the steep rise or decrease (Fig. 10.1). This hints at a charge effect in the ground with similarities to an electrical condenser. If a sinusoidal current is injected, one correspondingly observes a frequency dependence of apparent resistivity and a phase shift between current and voltage.

This phenomenon arises particularly at clay layers and metallic sulfides and oxides as well as graphite. One distinguishes between two mechanisms, *membrane* and *electrode polarization* (Fig. 10.2).

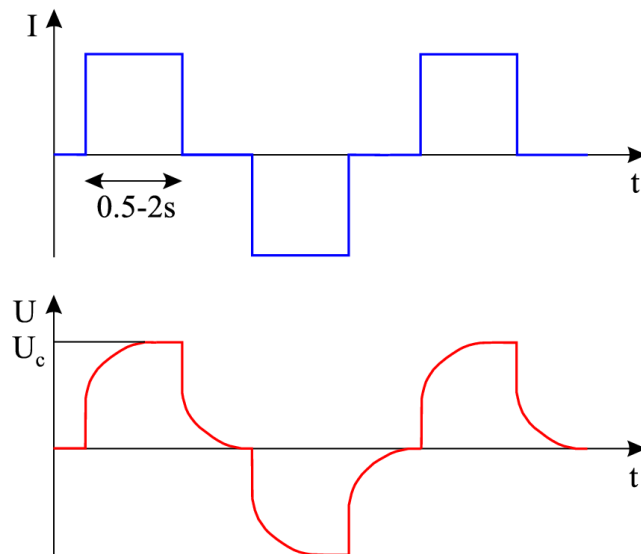


Fig. 10.1: Course of recorded potential difference (below) when an alternating DC current (above) is injected. Charge effects in the ground let the "target value" U_c be reached only after a certain time span.

Most rock-building minerals have a negative surface charge at the boundary to the pore fluid (Fig. 10.3). This results in a (very thin) layer of positive ions (cations), which are attached to the mineral surface (Stern layer). In bordering diffuse layer the number of freely movable cations decreases exponentially until equilibrium is reached with the anions. If the size of the pores is similar to the size of the Stern layer, an accumulation of charge carriers and a blocking of current flow is observed (Fig. 10.2a). Due to the large inner (specific) surface and corresponding small pore volume, this effect of membrane polarization is especially pronounced in clays. The method of Induced Polarization is thus particularly suited for the investigation of tightness of planned or existing waste deposits. However, the effect decreases with increasing fluid conductivity, e.g., with increased salinity¹.

Electrode polarization results from blocked pore space. With a voltage applied, positive and negative ions accumulate at each side of the grain; they either absorb electrons from the grain surface or dispense them to it. Because the velocity of electron transport is smaller than that of charge exchange with the ions, a built-up of charges occurs around the metal grain (Fig. 10.2b). If the external voltage is switched off, similarly to membrane polarization the ions diffuse gradually back to their original location.

¹ The formation of a double layer also leads to an increased current flow and thus an enhanced conductivity. The Archie formula of chapter 1 has thus to be extended by a term with this boundary layer conductivity.

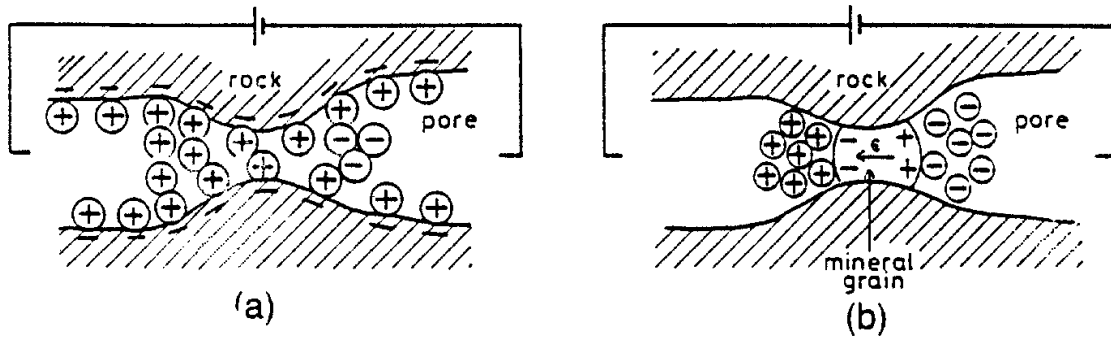


Fig. 10.2: Membrane (a) and electrode polarization (b).

In *Time Domain-IP* the voltage curve of Fig. 10.1 is analyzed by evaluating the area A beneath the decay curve between two times t_1 und t_2 (see Fig. 10.4):

$$M = \frac{1}{U_c} \int_{t_1}^{t_2} U(t) dt \quad (10.1)$$

The quantity M is called *chargeability*, measured in ms (sometimes only in mV/V, when the reference time is clear). Characteristic values are – at a recording time of $\Delta t = 1$ s – $M = 13.4$ ms for pyrite and $M = 2.2$ ms for magnetite.

In *Frequency-IP* an AC current of frequency f is injected². The normalized ratio

$$FE = \frac{\rho_0 - \rho_1}{\rho_0} \quad (10.2)$$

is called *frequency effect*; here ρ_0 is (apparent) DC resistivity and ρ_1 AC resistivity. In practice mostly a low frequency signal (e.g., $f = 1$ Hz) is used as approximation of the DC case and a just slightly higher frequency signal (e.g., $f = 10$ Hz) for determination of AC resistivity. The quantity

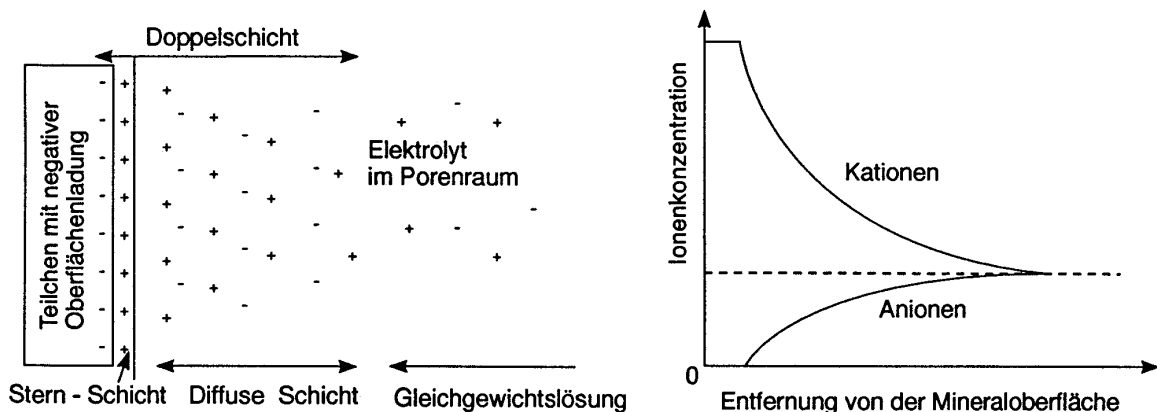


Fig. 10.3: Electric double layer at the boundary clay mineral-electrolyte. Left: distribution of ions, right: concentration of ions with distance from the surface (Radić in [KKL97]).

² In Frequency Domain-IP electromagnetic coupling, i.e., induction in cables may perturb. The effect is larger for large electrode separation and higher frequencies. Therefore a dipole-dipole configuration is better suited than a pole-pole or a pole-dipole spread.

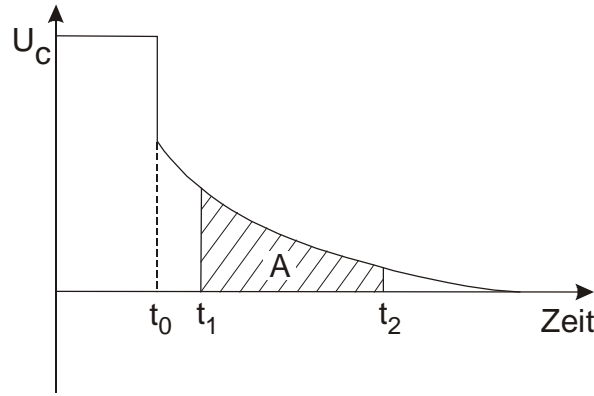


Fig. 10.4: Delineation of chargeability in time-domain IP.

$$\text{PFE} = 100 \text{ FE} \quad (10.3)$$

is then the *percentage frequency effect*. A *metal factor* is defined as:

$$\text{MF}_{\text{FD}} = 2\pi \cdot 10^5 \frac{\rho_0 - \rho_1}{\rho_1 \rho_0} \quad (10.4a)$$

In time domain a metal factor is known, too:

$$\text{MF}_{\text{TD}} = 2000 \frac{M}{\rho_0} \quad (\text{with } M \text{ in mV/V}). \quad (10.4b)$$

It thus has the dimension of conductivity in both cases.

As in the other electromagnetic methods, one may introduce an auxiliary circuit to illustrate the effects of induced polarization. It consists of a parallel circuit of a resistor with a serial circuit of a resistor and a capacitor (*Cole-Cole model*, Fig. 10.5). R_0 describes the DC part of resistance, $R_1 + Z(\omega)$ the lossy AC resistance:

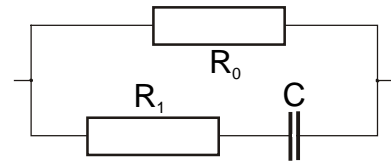


Fig. 10.5: Auxiliary circuit for the Cole-Cole model.

$$Z(\omega) = \left(\frac{1}{i\omega C} \right)^c \quad .$$

The constant c lies between 0 and 0.5; for $c = 0.5$, $Z(\omega)$ is called the *Warburg-Impedance*, the case Fall $c = 1$ corresponds to simple capacitor impedance. The total resistance $R(\omega)$ is then:

$$\frac{1}{R(\omega)} = \frac{1}{R_0} + \frac{1}{R_1 + Z(\omega)} \quad .$$

If we introduce:

$$m = \frac{R_0}{R_0 + R_1} \quad \text{und} \quad \tau = C \left(\frac{R_0}{m} \right)^{\frac{1}{c}} \quad ,$$

with the *Cole-Cole parameters* (which also comprise c) m = chargeability ($0 \leq m \leq 10$) and τ = time constant of relaxation, we arrive at the so-called *Cole-Cole equation*:

$$R(\omega) = R_0 \left\{ 1 - m \left[1 - \frac{1}{1 + (i \omega \tau)^c} \right] \right\} \quad (10.5)$$

Spectral IP is an extension of frequency domain IP; here complex resistivity (ρ_a and phase) as well as the Cole-Cole parameters are determined over a wide frequency range (approx. 0.1 – 1000 Hz).

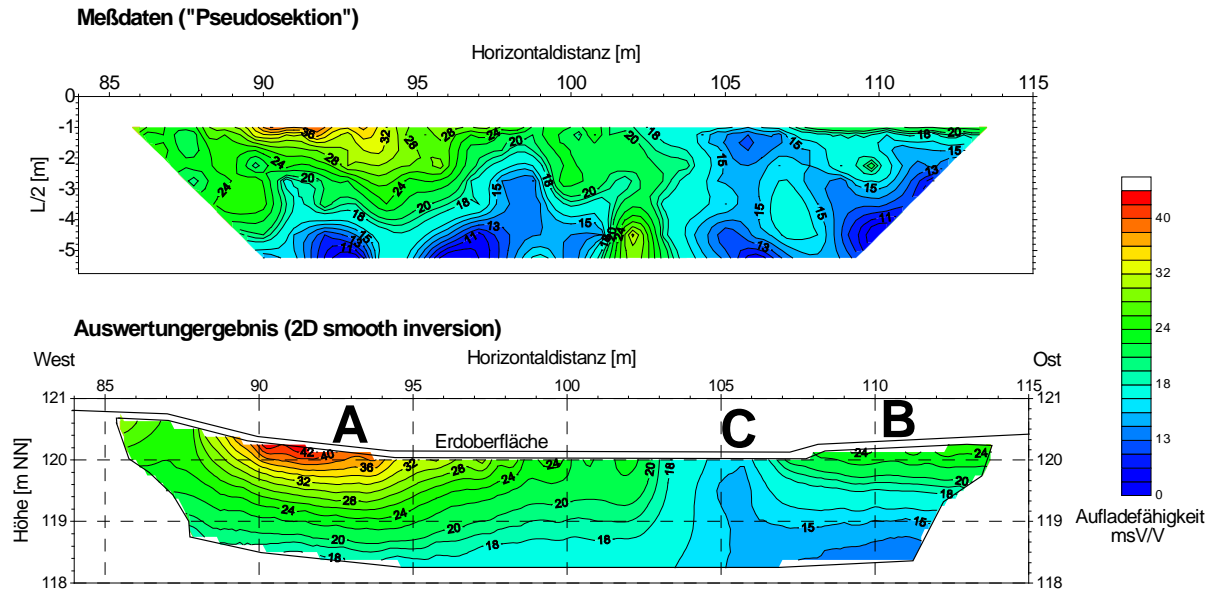


Fig. 10.6: Example of an IP sounding over a slag dump. Above: data, below: model of chargeability after inversion of the data set. With permission of Büro für Geophysik Berlin (BFG Lorenz), E. Niederleithinger.

11. Active induction methods in frequency and time domain

In this chapter we'll present a number of EM methods which use – different from MT and VLF – their own transmitter. The basic idea of frequency domain methods is always the following: A transmitter causes a (time-varying, usually monochrome) magnetic field in a Receiver. This field is composed of a primary field (the direct field of the transmitter) and the secondary field which originates from induction in the conducting earth or the anomalous body, respectively¹. Dependent on coupling (galvanic or inductive), transmitter-receiver configurations and layout of the receiver one distinguishes a large number of methods; from these we'll only discuss the *HLEM* (Horizontal Loop EM) or *Slingram method*. Here transmitter and receiver coils are coplanar to each other; the transmitted field is that of a vertical magnetic dipole.

Fig. 11.1 shows the principle HLEM scheme. The alternating current flowing in the primary circuit causes a magnetic field; this induces a primary field B_p in the secondary circuit. In the conducting anomaly eddy currents are induced which in turn give rise to a secondary magnetic field B_s in the receiver coil^{2,3}.

This figure already suggests the analogy with an AC current. One imagines the – now complex – resistivity of the anomaly as serial circuit of a purely ohmic and a purely inductive resistor (see Fig. 11.2). The total complex resistance is the calculated as

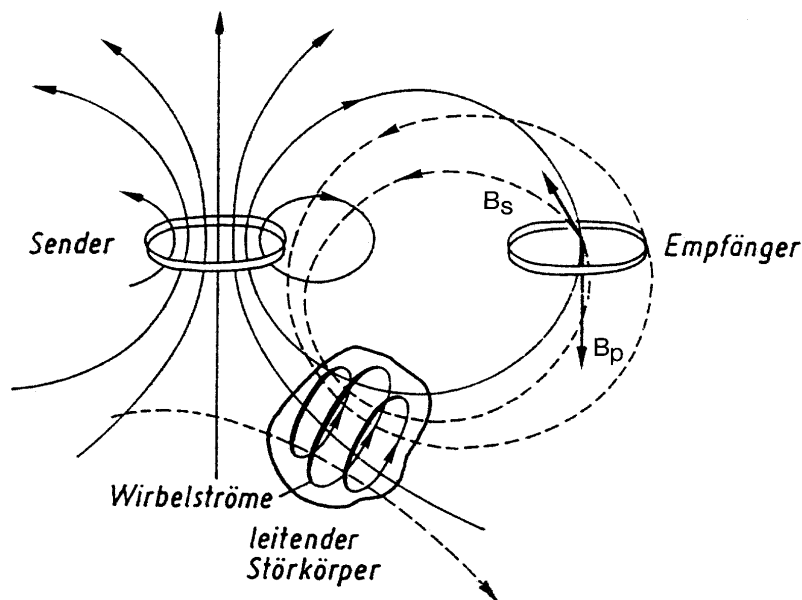


Fig. 11.1: magnetic field lines in the HLEM layout. B_p is the primary, B_s the secondary field at the location of the receiver coil. Modified after [MW85].

¹ Different to MT and VLF the fields in the methods treated here are inhomogeneous; the Helmholtz equation has to be complemented by a geometric term. Although CSAMT is an active method, too, analysis follows the standard MT procedure.

² The environment of the anomalous body is regarded as non-conductive in this approximation.

³ Also metal detectors often use the principle of active electromagnetics. Magnetometers are employed for this purpose, too, but their application is restricted to iron-containing objects.

$$R_G = R + i \omega L \quad , \quad (11.1a)$$

with ω as angular frequency (in Hz) and L as inductance (in Henry = Vs/A). A capacitive resistor does not have to be taken into account (charge effects don't play a role here). The dimension-less ratio

$$Q = \omega L/R \quad (11.1b)$$

is called *response parameter* or *induction number* of the perturbing body.

In the primary solenoid (transmitter) flows an alternating current $I_1 = I_{10} \exp(i \omega t)$; its magnetic field causes a magnetic flux Φ_{13} in the secondary solenoid (receiver) and a magnetic flux Φ_{12} in the anomaly:

$$\Phi_{12} = L_{12} I_1$$

$$\Phi_{13} = L_{13} I_1 \quad .$$

The L_{ij} are the so-called mutual inductances of the circuits i and j with $L_{ii} = L_i$ as inductance of circuit i . In the anomaly a voltage U_{12} is then induced (Faraday's law of induction), which in turn causes a current I_2 :

$$U_{12} = -\frac{d}{dt} \Phi_{12} = -i \omega L_{12} I_1$$

$$I_2 = \frac{U_{12}}{R_2 + i \omega L_2} = -\frac{i \omega L_{12} I_1}{R_2 + i \omega L_2} \quad .$$

This current leads to a flux Φ_{23} and a voltage U_{23} in the secondary coil:

$$\Phi_{23} = L_{23} I_2$$

$$U_{23} = -\frac{d}{dt} \Phi_{23} = -\omega^2 L_{12} L_{23} I_1 / (R_2 + i \omega L_2) \quad . \quad (11.2)$$

Direct coupling between transmitter and receiver yields:

$$U_{13} = -\frac{d}{dt} \Phi_{13} = -i \omega L_{13} I_1 \quad . \quad (11.3)$$

It thus follows for the ratio secondary/primary voltage:

$$\frac{U_{23}}{U_{13}} = -i \omega \frac{L_{23} L_{12}}{L_{13} (R_2 + i \omega L_2)} \quad (11.4a)$$

If so-called coupling

$$K_{ij} = \frac{L_{ij}}{\sqrt{L_i L_j}}$$

are introduced, then

$$\frac{U_{23}}{U_{13}} = -\frac{K_{12} K_{23}}{K_{13}} \frac{Q^2 + iQ}{1 + Q^2} = \Gamma \quad W \quad . \quad (11.4b)$$

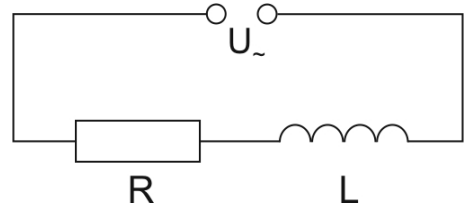


Fig. 11.2: AC circuit with ohmic resistance R and inductance L .

The – as Q dimension less – function

$$W = W(Q) = \frac{Q^2 + iQ}{1 + Q^2} \quad (11.5)$$

is called *response function*; its course is shown in Fig. 11.3 for real and imaginary part. At lower frequencies (i.e., $Q < 1$) the imaginary part dominates, for high frequencies ($Q > 1$) the real part⁴.

In the Slingram method the secondary field is measured in % of the primary field, ultimately the voltage ratio U_{23}/U_{13} from equations 11.4a and 11.4b, respectively. The phase relations are then (see also Fig. 11.4):

$$\Delta\theta = \theta_p - \theta_s = -\pi/2 + \arctan(\omega L/R) = -\pi/2 + \varphi \quad (11.6)$$

The primary field causes a phase shift of $-\pi/2$ (factor $-i$ in eq. 11.3) in the secondary circuit. The anomaly causes a further phase shift φ , which lies between 0° and $\pi/2$ depending on the ratio $Q = \omega L/R$. For poor conductors ($R \rightarrow \infty$) $\varphi \rightarrow 0^\circ$, for good conductors ($R \rightarrow 0$) $\varphi \rightarrow \pi/2$ ⁵. The total phase angle is thus between 90° and 180° .

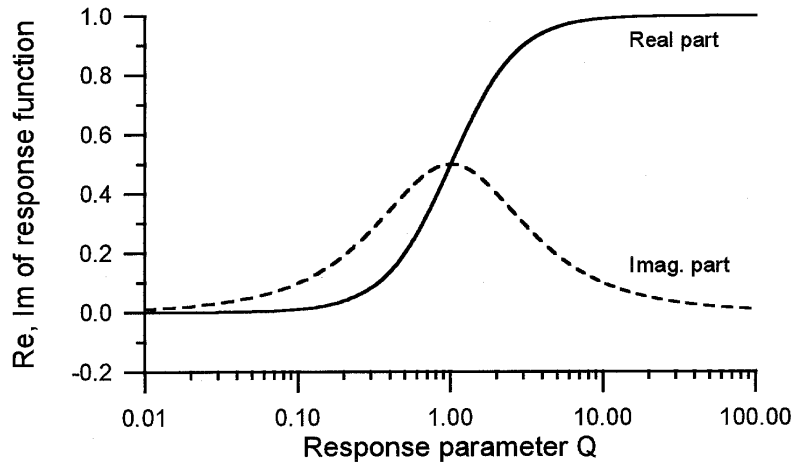


Fig. 11.3: Real and imaginary part of the response function in dependence of response parameter Q .

⁴ Many commercially available devices only allow measurements at a single frequency. But there exist devices which allow to measure at a number of frequencies; this enables a frequency-dependent depth sounding.

⁵ Note the similarity to the magnetotelluric phase shift between electric and magnetic field which also lies between 0° and 90° .

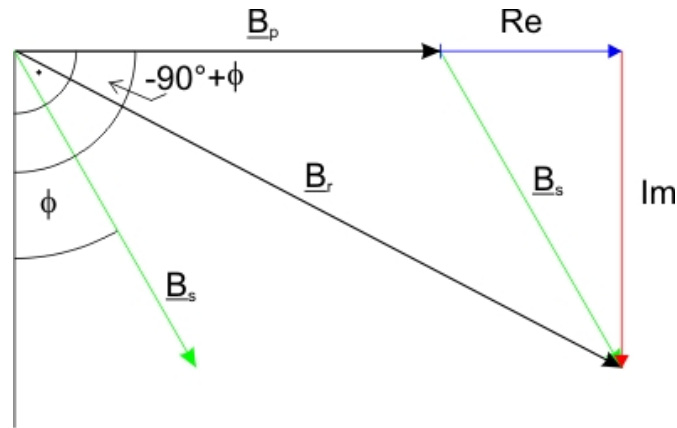


Fig. 11.4: Phase relations for the HLEM method. \underline{B}_r is the resulting field vector.

Fig. 11.5 shows the typical course of a Slingram profile over a plate-like anomaly. One always plots real part (*In-Phase*) and imaginary part (*Out-of-phase, Quadrature*) separately in relation to the primary field in %. For a better understanding the mutual coupling between the individual inductances is drawn in Fig. 11.6.

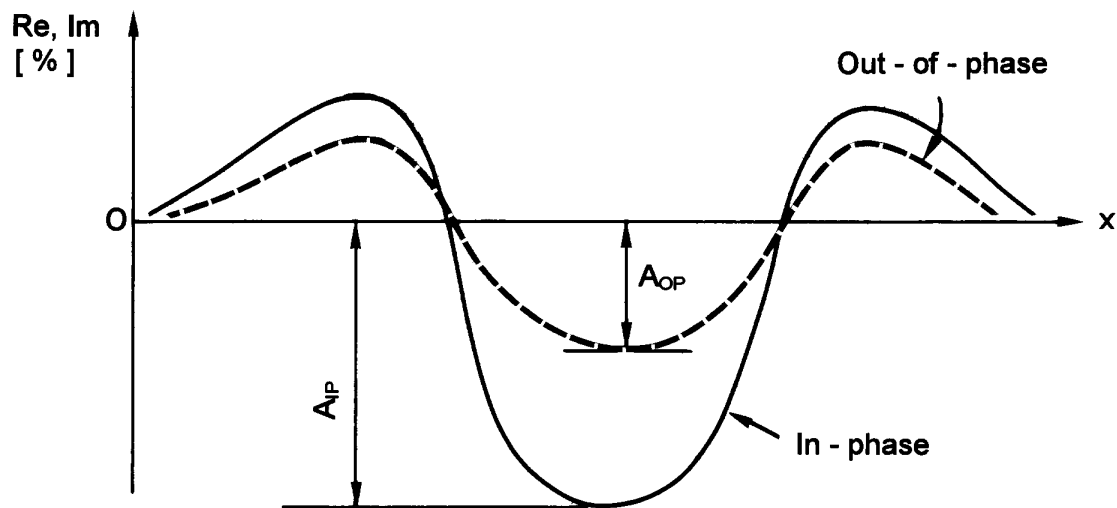


Fig. 11.5: Principle course of a HLEM (Slingram) anomaly at a fixed frequency. A_{IP} , A_{OP} : Amplitudes for In-phase and Out-of-phase.

The quantitative evaluation of such HLEM curves can't be detailed in the framework of this lecture. Instead we'll look at some model curves which enable an approximate interpretation for vertical or inclined sheets.

As parameter of induction process we introduced the response parameter Q (or induction number) in the circuit. Because we neither know the ohmic resistance of the anomalous body nor its inductance, we have to adapt the definition accordingly. One normally sets:

$$Q = \sigma \mu_0 \omega \Lambda^2 \quad (11.7)$$

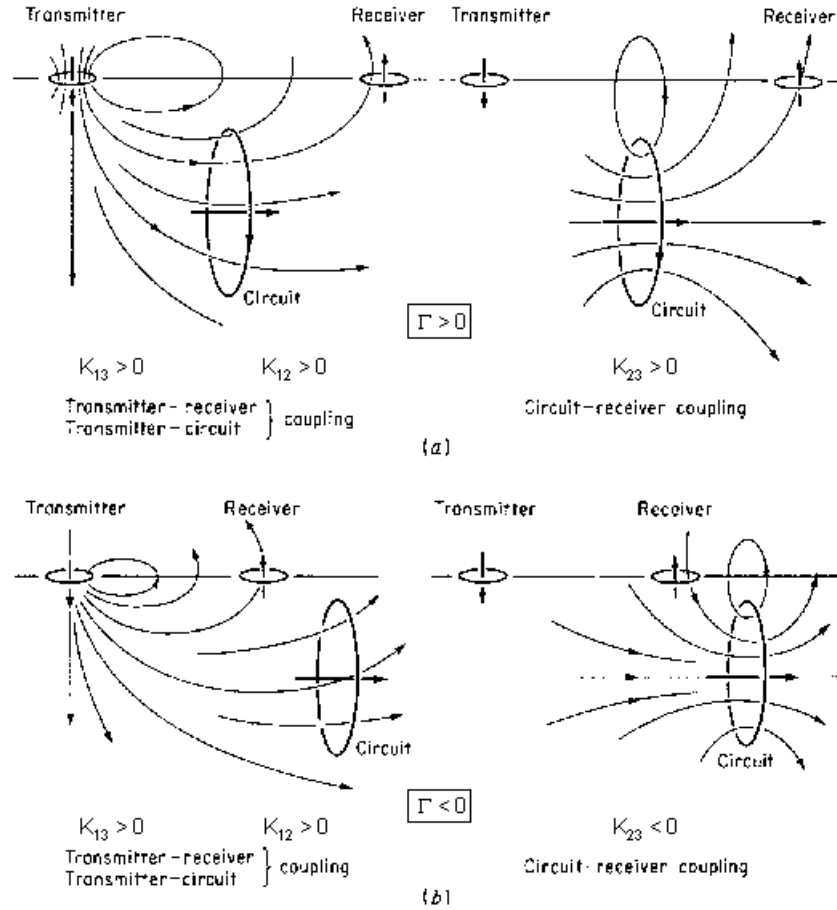


Fig. 11.6: Explanation of the course of a HLEM anomaly. (a) The conductor is located between transmitter and receiver, (b) the conductor is off the measurement system. K_{ij} are the mutual coupling factors, Γ is the combined coupling factor from eq. Gl. (11.4b). Modified from Grant & West (1965).

with: σ = electric conductivity of the anomalous body, ω = angular frequency, μ_0 = induction constant and Λ = characteristic length of the measurement system or the anomalous structure, respectively. For a vertical sheet:

$$Q = \sigma \mu_0 \omega \ell d \quad ; \quad (11.8)$$

here d = thickness of the plate and ℓ = separation transmitter-receiver. The definition of Q looks arbitrary at first glance but becomes clearer when we look at Q as the ratio of a characteristic length Λ of the measurement system (or subsurface model) and skin depth $\delta = (2/\sigma \mu_0 \omega)^{1/2}$: $Q = \Lambda/\delta$ with $\Lambda = 2 \ell d/\delta$.

The amplitudes of the anomaly are first determined according to Fig. 11.5. They are then plotted into the *Argand diagrams* (Quadrature value as ordinate, In-phase part as abscissa, with induction number Q and ratio z/ℓ as parameter, in which z = depth of upper plate limit) for the respective dip angles (Fig. 11.7, the induction numbers are denoted as p here). The induction number may then be read. It often suffices to interpolate Q linearly between the parameter curves. The conductance $\tau = \sigma d$ is then determined from the defining equation of Q above. The ratio z/ℓ may be read from the Argand diagrams, too, from which z is obtained.

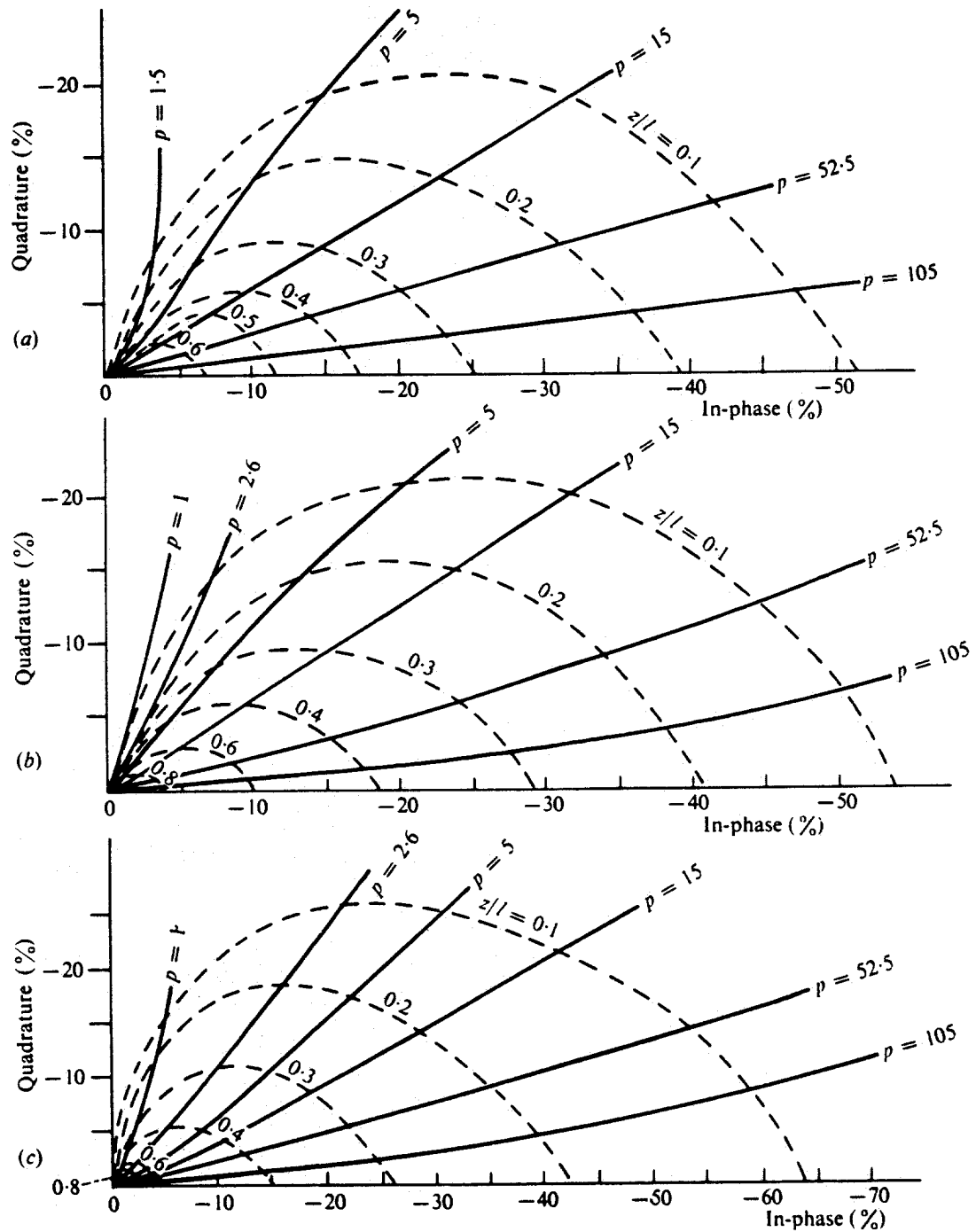


Fig. 11.7: Characteristic curves for HLEM systems, measured above a plate with different dip angles. a) Angle 90° (vertical plate), b) 60°, c) 30°. z/l : ratio depth of top upper plate to transmitter-receiver separation, p induction parameter. After Strangway (1966) and Telford et al. (1992).

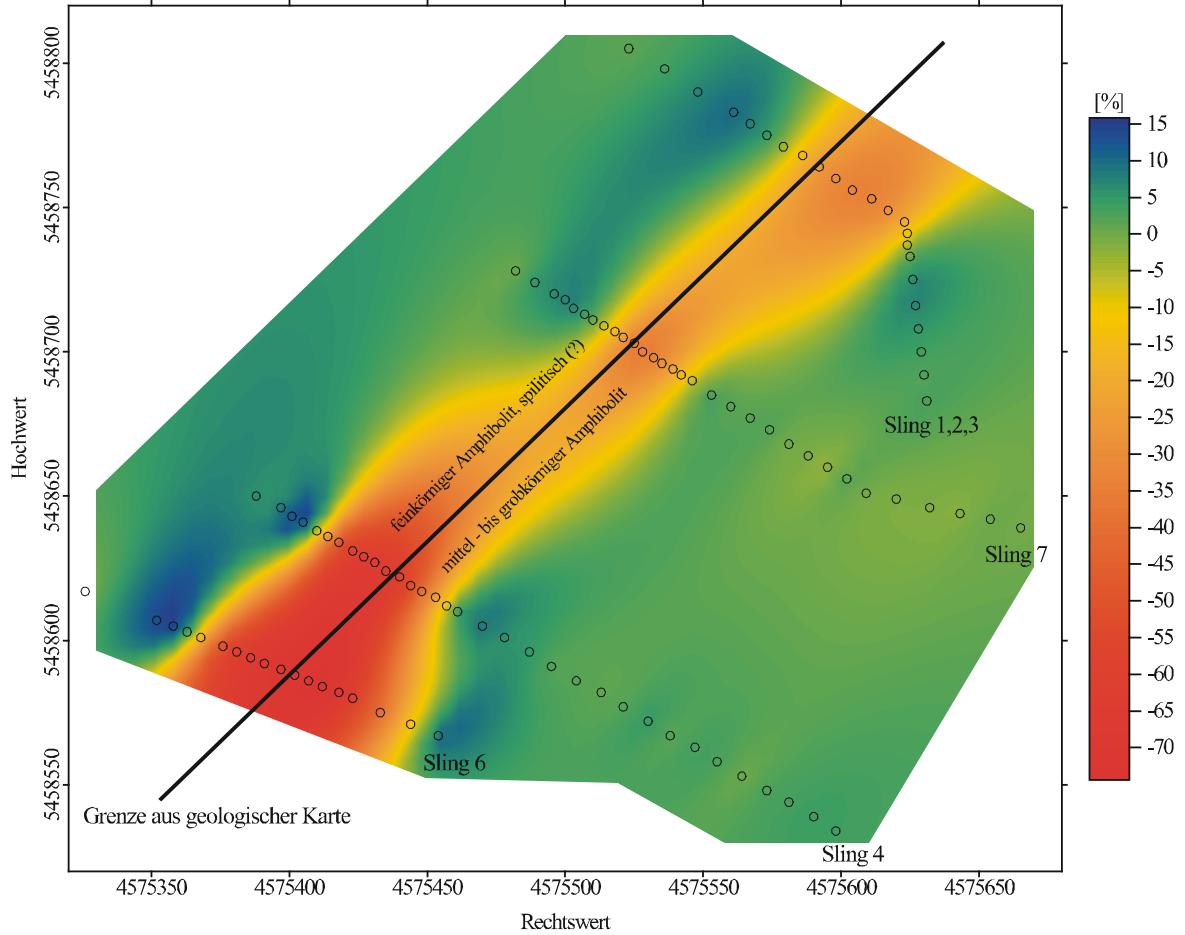


Fig. 11.8: Example of a Slingram anomaly (in-phase) along a fault zone in the Bohemian Forest near the border Germany/Czech Republic. Excursion report FU Berlin 1998.

In limiting cases the conductivity distribution may be delineated from the ratio secondary to primary field (to be more exact: from the quadrature term), namely when the system is operated at small induction numbers, i.e.:

$$\omega \ll \frac{2}{\mu_0 \sigma \ell^2} \quad ,$$

the T-R separation ℓ is much smaller than skin depth δ . Then:

$$\sigma_a = \frac{4}{\mu_0 \omega \ell^2} \left(\frac{B_s}{B_p} \right)_{\text{Quad}} \quad . \quad (11.9)$$

One may take advantage of this particularly in a system where the coils are mounted on a rod; such a system may even be operated by a single person.

The horizontal loop configuration is the most conventional of active FD EM, but other variations are possible, too. An overview is given in Fig. 11.9.

A concluding remark: The active, purely magnetic methods are particularly important in aero-geophysical research (see Fig. 11.10). Another application is the *induction log* in boreholes.

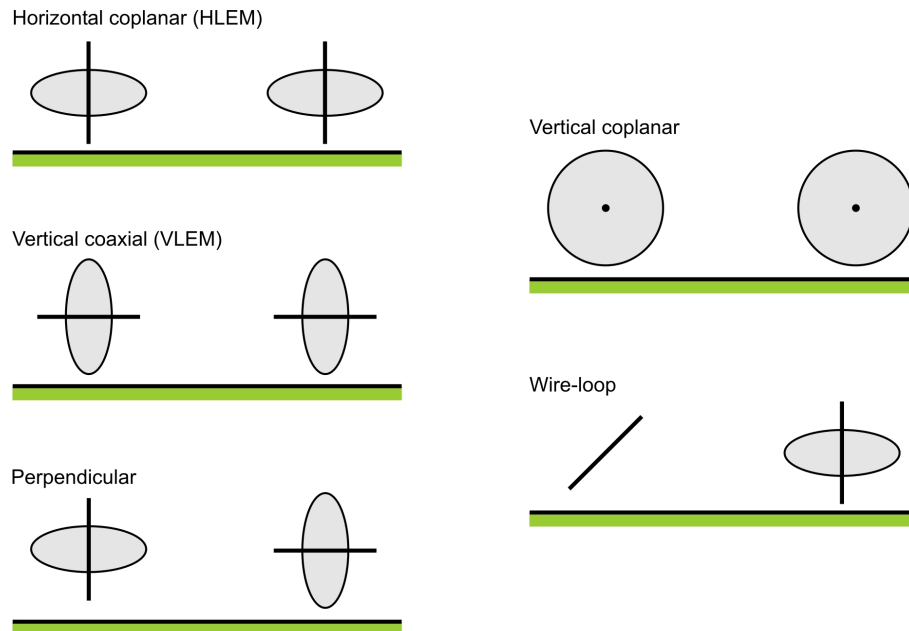


Fig. 11.9: Possible configurations of active frequency domain electromagnetics.

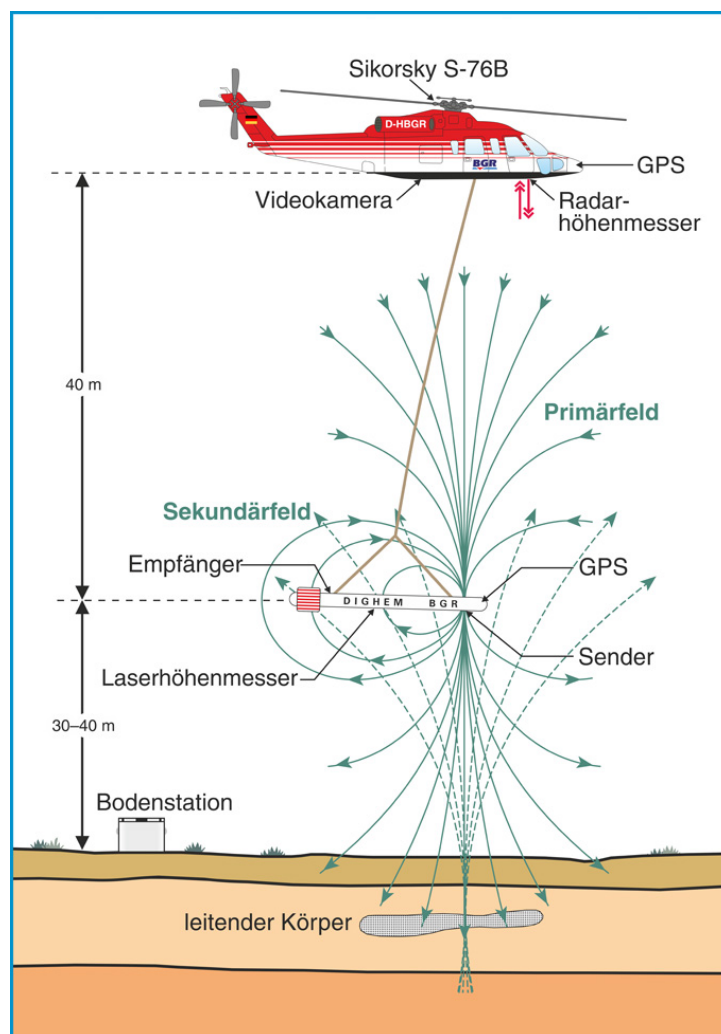


Fig. 11.10: Helicopter EM (B. Siemon, Federal Institute for Geosciences and Natural Resources, Hannover: http://www.bgr.bund.de/EN/Home/homepage_node_en.html).

Electromagnetic methods in time domain are summarized under the name *Transient Electromagnetics (TEM)*, also *TDEM* for *Time Domain Electromagnetics*; here the decay curve after switch-off of the transmitter current is measured in a receiver coil. The transmitter coil is usually rectangular with an edge length of 5-100 m (also grounded electrical dipoles are in use). By switching off the transmitter, currents are induced in the conducting ground; they propagate downwards and to the sides and decay rapidly. The decay time is determined by the conductivity of the subsoil (see Figs. 11.11 und 11.12).

This current system generates a secondary magnetic field that is recorded in a receiver coil at the surface sequentially at times t_1, \dots, t_n . The principal advantage (concerning measurement technique) with respect to other active electromagnetic methods is that the decay curve (which is sampled for time spans between several μs to several 100 ms) is not superimposed by the much stronger primary field. By recording at different times a deep sounding is achieved analogously to the FD methods.

The temporal variation of the vertical magnetic field $\partial B_z / \partial t$ (with a horizontal receiver coil) is a complicated function of a dimensionless time parameter

$$\tau = \frac{t}{\mu_0 \sigma a^2} \quad (11.10)$$

with μ_0 = induction constant, σ = electrical conductivity, a = radius of transmitter coil and t the time after current cut off. It holds (for a detailed derivation see, e.g., Ward & Hohmann 1987):

$$\frac{\partial B_z}{\partial t} = \frac{-I}{\sigma a^3} \left[3 \operatorname{erf} \left(\frac{1}{2\sqrt{\tau}} \right) - \frac{1}{\sqrt{\pi \tau}} \left(3 + \frac{1}{2\tau} \right) e^{-\frac{1}{4\tau}} \right]$$

with the error function $\operatorname{erf} x$ (Fig. 11.13):

$$\operatorname{erf} x = \frac{2}{\sqrt{\pi}} \int_0^x e^{-y^2} dy \quad .$$

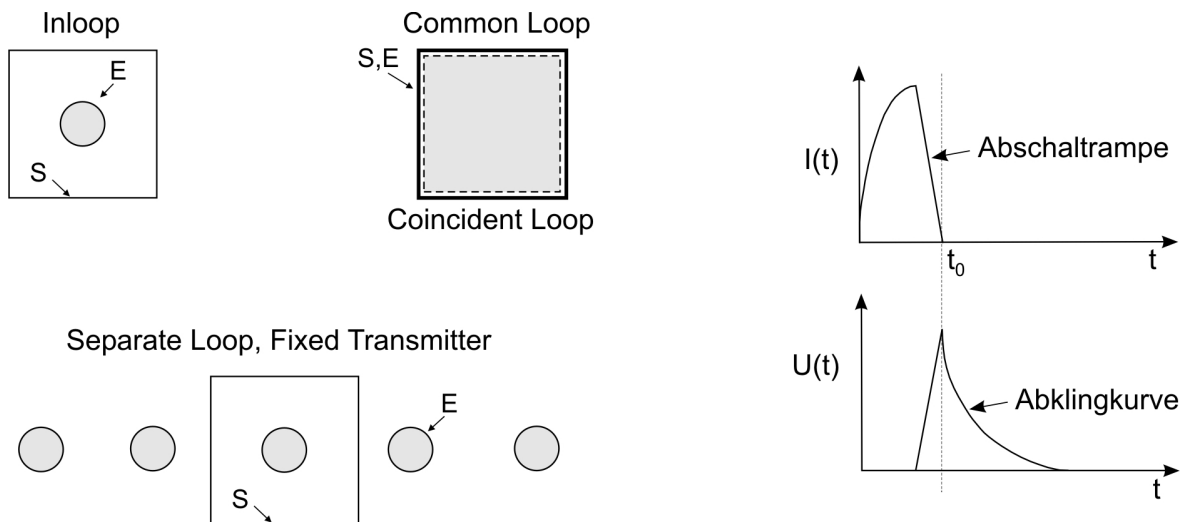


Fig. 11.11: Common transmitter-receiver configurations in TEM (left). Right: Course of transmitter current and induced voltage.

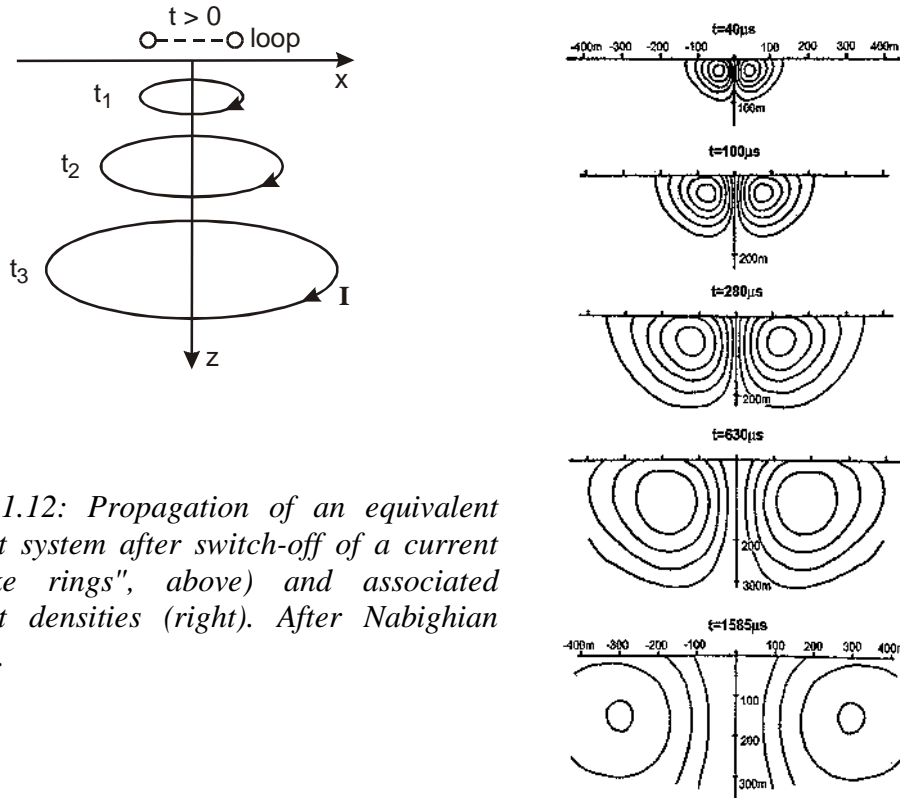


Fig. 11.12: Propagation of an equivalent current system after switch-off of a current ("smoke rings", above) and associated current densities (right). After Nabighian (1979).

The error function is the integral of Gauss normal distribution and gives the probability that the normally distributed random variable y takes maximal the value x .

For *early times* ($\tau \ll 1$) and *late times* ($\tau \gg 1$), respectively, simple expressions may be derived:

$$\frac{\partial B_z}{\partial t} = \frac{3I}{\sigma a^3} \quad \text{für } \tau \ll 1 \quad (15.11a)$$

$$\frac{\partial B_z}{\partial t} = \frac{Ia^2}{20} \sqrt{\frac{\sigma^3 \mu_0^5}{\pi t^5}} \quad \text{für } \tau \gg 1. \quad (15.11b)$$

For early times the measured magnetic field variation is thus inversely proportional to conductivity and independent of time t (horizontal branch of the decay curve, Fig. 11.14), for late times $\partial B_z / \partial t$ is proportional to $\sigma^{3/2}$ and decays with $t^{5/2}$.

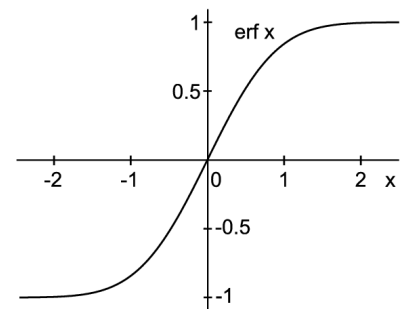


Fig. 11.13: Course of $\text{erf } x$

Curves of apparent resistivity $\rho_a(t)$ as function of decay time can also be plotted for TEM; however they are split into early and late times and thus less intuitive than corresponding curves in DC geoelectrics or MT.

TEM is employed in environmental geophysics and studies of the uppermost crust; however, with sufficient transmitter currents it may also be applied for studies of the mid crust (*LOTEM Method*, from Long Offset TEM) and due to the purely magnetic excitation and recording it is also conventionally applied in aero-geophysics.

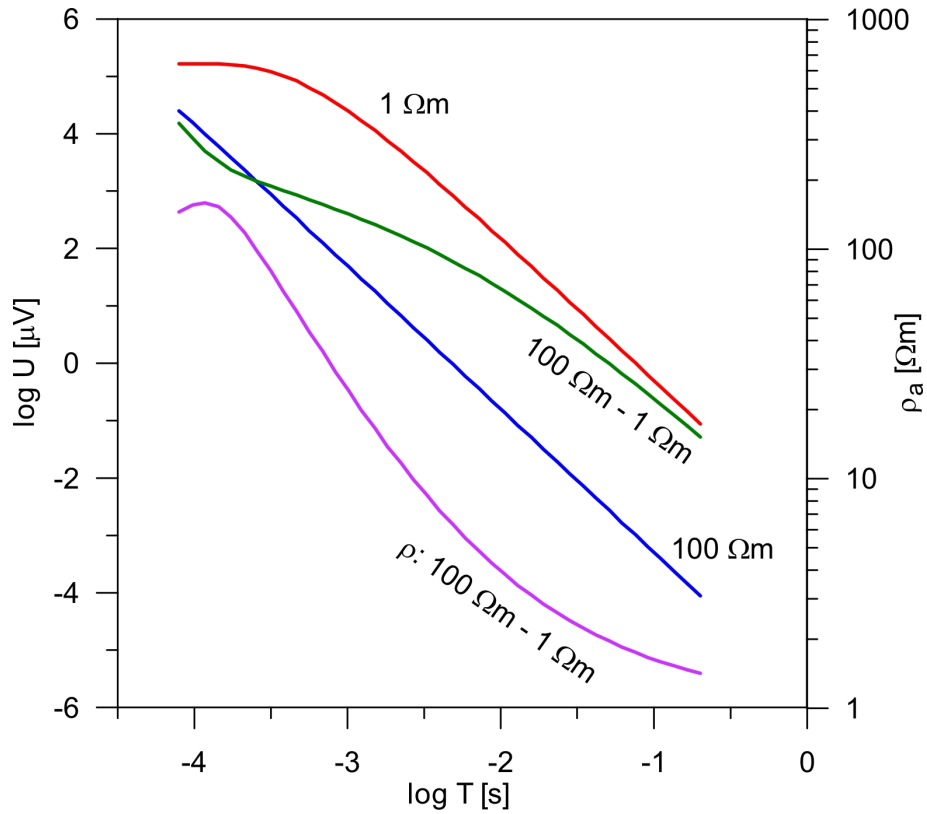


Fig. 11.14: Examples of decay curves (Sirotem instrument, calculated with a program by P. Weidelt and S. Greinwald, BGR Hannover) for a homogeneous half space of $100 \Omega m$ (blue) and $1 \Omega m$ (red) and a layered half space (100 m thick overburden with $\rho = 100 \Omega m$ above a substratum with $\rho = 1 \Omega m$). Violet: ρ_a -curve for the third case. Edge length of rectangular coil = 100m, Coincident Loop configuration.

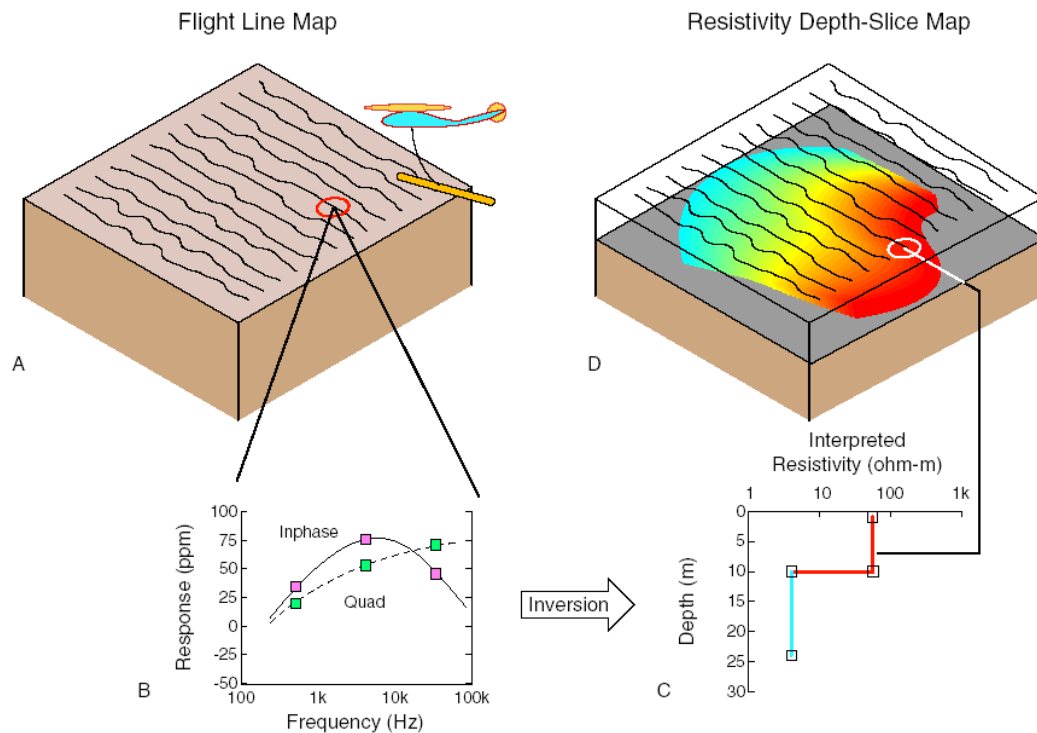


Fig. 11.15a: Example of helicopter electromagnetics (source: USGS).



Fig 11.15b: Layout of aero-electromagnetic devices. Links: Bird at a helicopter, right top: TEM-System (Fugro Airborne Surveys, www.fugroairborne.coft.au/index.shtml), right below: Helicopter-TEM to detect UXO (unexploded – also unexplored – ordnance) (Oak Ridge Airborne Geophysical System, from: Beard et al., Geophysics, 69, 2004).

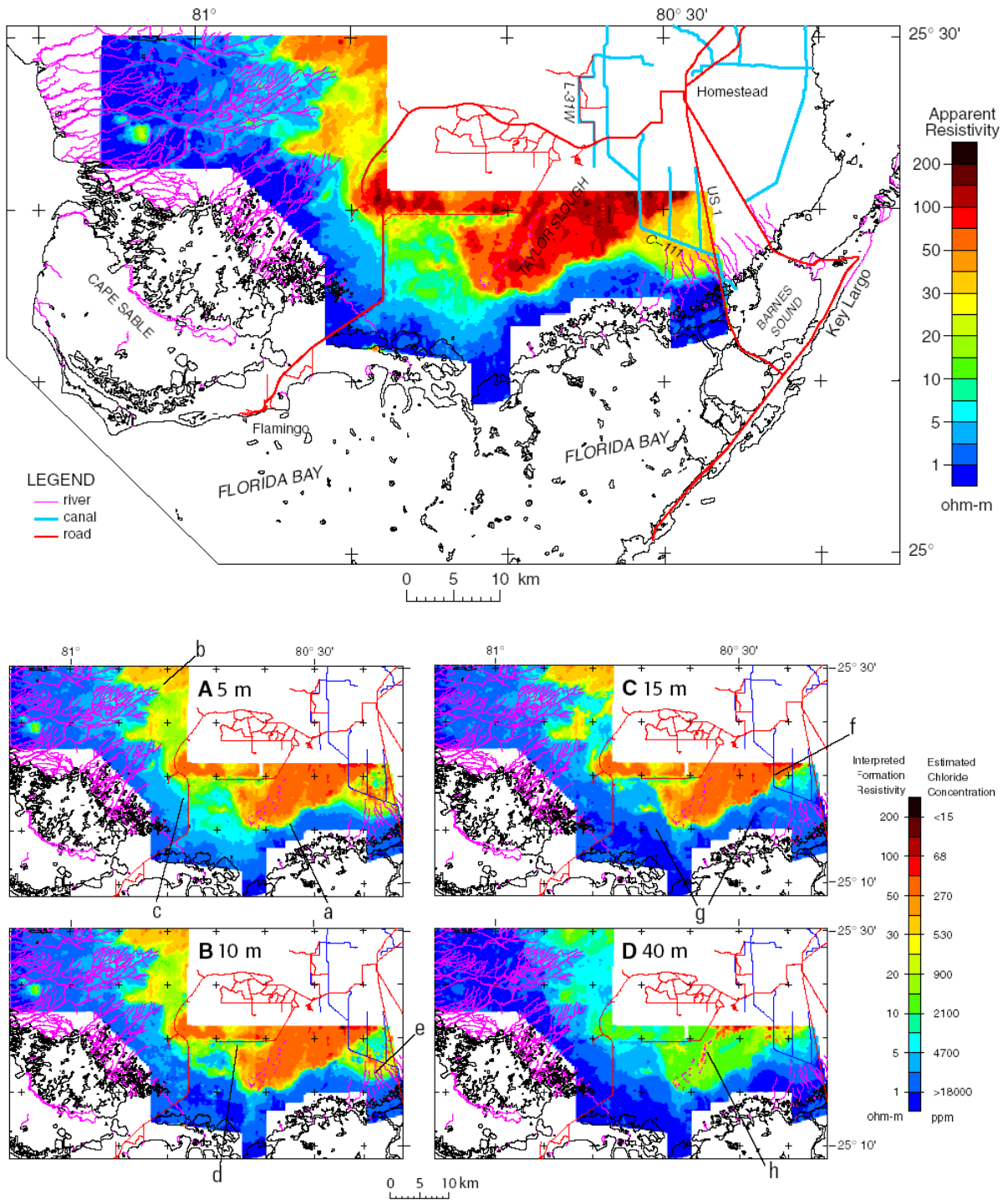


Fig. 11.16: Salt water intrusion in the Everglades, Florida: Results of helicopter EM (source: USGS).